Федеральное государственное автономное образовательное учреждение
высшего образования
«Московский физико-технический институт
(национальный исследовательский университет)»
Физтех-школа физики и исследований им. Ландау
Кафедра физики высоких энергий

Направление подготовки / специальность: 03.04.01 Прикладные математика и физика
Направленность (профиль) подготовки: Общая и прикладная физика

ИЗМЕРЕНИЕ ЭФФЕКТИВНОСТИ МЕЧЕНИЯ BS/ANTI-BS МЕЗОНОВ В МОМЕНТ РОЖДЕНИЯ С ПОМОЩЬЮ БЫСТРЫХ ЗАРЯЖЕННЫХ КАОНОВ В ЭКСПЕРИМЕНТЕ АТЛАС

(магистерская диссертация)

Студент:
Манасавала Хусайн Мустансир

_____
(подпись студента)

Научный руководитель:
Николаенко Владимир Иванович,
канд. физ.-мат. наук

_____
(подпись научного руководителя)

Консультант *(при наличии)*:
_____
_____
(подпись консультанта)

Москва 2022

Acknowledgements

Я хотел бы поблагодарить Николаенко Владимира Ивановича за научное руководство, помощь с реализацией этой работы и освоением программных методов, использованных в ходе этой диссертации. Также выражаю благодарность сотрудникам лаборатории фундаментальных взаимодействий, МФТИ и коллегам BsJpsiPhi группы коллаборации АТЛАС в ЦЕРН за предоставление нужных данных, доступа к вычислительным кластерам и за их помощь с освоением интерфейса программы парциально-волнового анализа и обсуждения разных возникающих вопросов за последние два года.

Благодарю Зайцеву Александру Михайловичу за его помощь с переходом в физику высоких энергий, подготовкой до поступления на кафедру и освоением нужных материалов, Мягкову Алексею Григорьевичу за лекции по статистическим методам в физике высоких энергий и Root.

Огромное спасибо моему товарищу Бородулину Ивану Сергеевичу за всю его помощь, кураторство и дружбу.

Abstract

The B_s system rapidly oscillates between its particle ($\overline{b}s$) and antiparticle ($b\overline{s}$) states with a frequency of 17.7ps^{-1}. In this thesis, a same-side tagging algorithm is developed to determine the initial composition of B_s mesons decaying as $B_s \to J/\psi(\to \mu^+\mu^-)\phi(\to K^+K^-)$, the charge of fast moving kaons formed using the second strange quark of a sea $s\overline{s}$ pair which contributes to the formation of the signal B_s is the main factor, determining the flavouring at the moment of creation. A correct identification of the initial composition is fundamental in measurements such as time-dependent CP-violation asymmetries of $B_s^0 \leftrightarrow \overline{B}_s^0$ oscillations. Both these type of measurements are exploited by the ATLAS experiment in the research of new physics Beyond the Standard Model. The developed technique is compared to other available tagging algorithms such as opposite side electron and muon tagging. The goal of the study is measurement of the qualifying parameters of the new same-side tagger, efficiency ϵ, dilution $\mathcal{D}$, and tagging power T, as well as the CP-violation phase ϕ_s in the CKM formalism, decay width Γ, width and mass differences $\Delta\Gamma_s$, Δm_s through a partial wave analysis fit. The measured values and statistical errors on them are:

$$\begin{aligned}
\epsilon &= 1.92 \pm 0.11 \text{ (stat.)}\% \\
\mathcal{D} &= 70.69 \pm 4.97 \text{ (stat.)}\% \\
T &= 0.95 \pm 0.19 \text{ (stat.)}\% \\
\phi_s &= -0.0080 \pm 0.0294 \text{ (stat.) [rad]} \\
\Gamma_s &= +0.6722 \pm 0.0011 \text{ (stat.) [ps}^{-1}\text{]} \\
\Delta\Gamma_s &= +0.0645 \pm 0.0034 \text{ (stat.) [ps}^{-1}\text{]} \\
\Delta m_s &= +17.8999 \pm 0.1383 \text{ (stat.) [ps}^{-1}\text{]}
\end{aligned}$$

Contents

Chapter 1

Introduction and Motivation

In this chapter, a brief description of the Standard Model (SM) of particle physics is laid out. An introduction to CP-violation and flavour tagging are also given in sections 1.3 and 1.4 to convey the motivation for this study.

1.1 The Standard Model

The Standard Model of particle physics is a spontaneously broken Yang-Mills quantum field theory, that combines the principles of special relativity with quantum theory into a mathematical framework that describes the interactions of fundamental particles through strong, weak and electromagnetic interactions based on the local gauge symmetry group:

$$G_{SM} \equiv SU(3)_C \times SU(2)_L \times U(1)_Y$$

A notable outlier is gravitation, the possibility of the inclusion of which into an all encompassing theory is yet an open question in physics of the highest importance. Gravity is hypothesised in prominent theories to be mediated by a single spin-2 bosonic tensor field, termed 'the graviton'.

Along with the gauge bosons that mediate the fundamental forces, and the scalar Higgs sector the spectrum of the Standard Model Lagrangian contains the following matter fields and transformation properties (where the index i labels the quark and lepton generations as $i = 1, 2, 3$):

$$\begin{aligned} Q_i &\equiv \begin{pmatrix} u_{L_i} \\ d_{L_i} \end{pmatrix} \sim (3, 2, \tfrac{1}{6}) & U_i &\equiv u_{R_i} \sim (\overline{3}, 1, \tfrac{2}{3}) \\ L_i &\equiv \begin{pmatrix} \nu_{L_i} \\ e_{L_i} \end{pmatrix} \sim (1, 2, -\tfrac{1}{2}) & D_i &\equiv d_{R_i} \sim (\overline{3}, 1, -\tfrac{1}{3}) \\ H_i &\equiv \begin{pmatrix} H^+ \\ H^0 \end{pmatrix} \sim (1, 2, \tfrac{1}{2}) & E_i &\equiv e_{R_i} \sim (1, 1, -1) \end{aligned}$$

The Lagrangian of the Standard Model may be represented as follows:

$$\mathcal{L}_{SM} = \mathcal{L}_F + \mathcal{L}_{YM} + \mathcal{L}_{yukawa} + \mathcal{L}_S$$

where

$$\begin{aligned}
\mathcal{L}_F &= i\overline{\Psi}\gamma^\mu D_\mu \Psi,\ \Psi \equiv (Q_i, U_i, D_i, L_i, E_i) \\
D_\mu &= \partial_\mu - ig_s G^A_\mu \lambda^A - i\frac{g}{2} W^I_\mu \tau^I - ig' B_\mu Y \\
\mathcal{L}_{YM} &= -\frac{1}{4} G^{\mu\nu A} G^A_{\mu\nu} - \frac{1}{4} W^{\mu\nu I} W^I_{\mu\nu} - \frac{1}{4} B^{\mu\nu} B_{\mu\nu} \\
G^A_{\mu\nu} &= \partial_\mu G^A_\nu - \partial_\nu G^A_\mu + g_s f_{ABC} G^B_\mu G^C_\nu \\
W^I_{\mu\nu} &= \partial_\mu W^I_\nu - \partial_\nu W^I_\mu + g f_{IJK} W^J_\mu W^K_\nu \\
B_{\mu\nu} &= \partial_\mu B_\nu - \partial_\nu B_\mu \\
\mathcal{L}_{yukawa} &= h^u_{ij} \overline{Q}_i U_j (i\sigma^2 H^*) + h^d_{ij} \overline{Q}_i D_j H + h^e_{ij} \overline{L}_i E_j H + h.c. \\
\mathcal{L}_S &= (D_\mu H)^\dagger D_\mu H - \mu^2 H^\dagger H - \lambda (H^\dagger H)
\end{aligned} \tag{1.1}$$

Where, $A = 1, 2, 3 \ldots 8$ and G^A_μ represent the $SU(3)_C$ gauge bosons, $I = 1, 2, 3$ and W^I_μ the $SU(2)_L$, and B_μ the $U(1)_Y$ fields. The $SU(3)$ and $SU(2)$ structure constants are represented by f_{ABC} and f_{IJK} respectively. The coupling constants in the $\mathcal{L}_{yukawa}$ term are responsible for the masses of the fermions through the Higgs mechanism as the Standard Model symmetry spontaneously breaks as $G_{SM} \to SU(3)_C \times U(1)_{em}$, while allowing the Standard Model to be a non-anomalous renormalisable theory.

The electroweak bosons are decoupled by the Higgs mechanism to yield the the photon γ (gauge field A_μ) and three weak bosons (gauge fields $W^\pm_\mu$ and Z_μ):

$$\begin{aligned}
W^\pm_\mu &= \frac{W^1_\mu \pm W^2_\mu}{\sqrt{2}} \\
Z_\mu &= \cos\theta_W W^3_\mu + \sin\theta_W B_\mu \\
A_\mu &= -\sin\theta_W W^3_\mu + \cos\theta_W B_\mu
\end{aligned} \tag{1.2}$$

Where θ_W is the Wienberg angle defined as $\arctan g'/g$, with g', g being the $SU(2)_L$ and $U(1)_Y$ couplings.

A relativistic, Lorentz-invariant, local quantum field theory with a hermitian Hamiltonian, as per the CPT-Theorem, must be symmetric under simultaneous action of the charge conjugation operator C, parity transformation or spatial inversion P, and time reversal T. The theorem also requires particles and corresponding antiparticles to have equal masses and decay times.

1.2 The Cabbibo-Kobayashi-Maskawa Formalism

The masses and mixing of the quarks arise from the Yukawa interactions of the quarks with the Higgs field as shown in $\mathcal{L}_{yukawa}$. The Yukawa couplings $h_{ij}^{u,d}$ are 3×3 complex matrices. When the Higgs field acquires a vacuum expectation value $v/\sqrt{2} : v = \sqrt{\mu^2/\lambda}$ these couplings yield mass terms for the quarks. The mixing results from the fact that the interaction eigenstates of the quarks differ from their mass eigenstates. If we consider the weak interaction Lagrangian [1]:

$$\mathcal{L}_W = -\frac{g}{\sqrt{2}} W^+ \overline{u}_{L_i}^I \gamma_\mu \mathbb{I} d_{L_i}^I + h.c. \tag{1.3}$$

noting that the $\mathbb{I}$, identity matrix is there to underline that the weak interactions are diagonal in the weak-eigenstate basis, in which the quarks are doublets Q_i to the $SU(2)_L$ and singlets U_i, D_i to $U(1)_Y$. The coupling matrices $h_{ij}^{u,d}$ in the SM are not simultaneously diagonalisable [2]. The resultant mass terms are:

$$m_{u_i} = \frac{h^u v}{\sqrt{2}} \qquad m_{d_i} = \frac{h^d v}{\sqrt{2}} \tag{1.4}$$

The physical states are therefore obtained by diagonalising the coupling matrices with the help of four unitary matrices $V_{L,R}^{u,d}$ as

$$M_{diag} = V_L^q h^q V_R^q \frac{v}{\sqrt{2}} \tag{1.5}$$

with $q = u, d$. This leads to the charged current $W^\pm$ interactions being coupled to the physical (mass) eigenstates as ($V_{CKM} \equiv V_L^u V_L^{d\dagger}$):

$$-\frac{g}{\sqrt{2}} (\overline{u}_L, \overline{c}_L, \overline{t}_L) \gamma_\mu W^+ V_{CKM} \begin{pmatrix} d_L \\ s_L \\ b_L \end{pmatrix} \qquad V_{CKM} = \begin{pmatrix} V_{ud} & V_{us} & V_{ub} \\ V_{cd} & V_{cs} & V_{cb} \\ V_{td} & V_{ts} & V_{tb} \end{pmatrix} \tag{1.6}$$

This is the Cabibbo-Kobayashi-Maskawa matrix, which relates the mass and interaction eigenstates as:

$$\begin{pmatrix} d' \\ s' \\ b' \end{pmatrix} = \begin{pmatrix} V_{ud} & V_{us} & V_{ub} \\ V_{cd} & V_{cs} & V_{cb} \\ V_{td} & V_{ts} & V_{tb} \end{pmatrix} \begin{pmatrix} d \\ s \\ b \end{pmatrix} \tag{1.7}$$

It is evident that this matrix is unitary, which eliminates the possibility of flavour changing neutral currents (FCNC). The unitary conditions are:

$$\sum_{k=1} V_{ki}V_{kj}^* = \delta_{ij} \qquad \sum_{k=1} V_{ik}V_{jk}^* = \delta_{ij} \tag{1.8}$$

These conditions reduce the $2n^2$ real parameters that define an arbitrary $n \times n$ matrix to n^2, and $2n-1$ phases can be eliminated through redefinition of the quark fields, leaving $(n-1)^2$ independent parameters, which in the given case of $n = 3$, results in four parameters. Following the Particle Data Group [2] we may parameterise the matrix with three mixing angles and a phase as follows:

$$V_{CKM} = \begin{pmatrix} c_{12}c_{13} & s_{12}c_{13} & s_{13}e^{-i\delta} \\ -s_{12}c_{23} - c_{12}s_{23}s_{13}e^{i\delta} & c_{12}c_{23} - s_{12}s_{23}s_{13}e^{i\delta} & s_{23}c_{13} \\ s_{12}s_{23} - c_{12}c_{23}s_{13}e^{i\delta} & -c_{12}s_{23} - s_{12}c_{23}s_{13}e^{i\delta} & c_{23}c_{13} \end{pmatrix} \tag{1.9}$$

where $c_{ij} = \cos\theta_{ij}$ and $s_{ij} = \sin\theta_{ij}$. This can be broken down as:

$$V_{CKM} = \begin{pmatrix} 1 & 0 & 0 \\ 0 & c_{23} & s_{23} \\ 0 & -s_{23} & c_{23} \end{pmatrix} \cdot \begin{pmatrix} c_{13} & 0 & s_{13}e^{i\delta} \\ 0 & 1 & 0 \\ -s_{13}e^{i\delta} & 0 & c_{13} \end{pmatrix} \cdot \begin{pmatrix} c_{12} & s_{12} & 0 \\ -s_{12} & c_{12} & 0 \\ 0 & 0 & 1 \end{pmatrix} \tag{1.10}$$

It has been experimentally determined that $s_{13} \ll s_{23} \ll s_{12}$, which is expressed in the popular Wolfenstein parametrisation, where we define:

$$\lambda \equiv s_{12} = \frac{|V_{us}|}{\sqrt{|V_{ud}|^2 + |V_{us}|^2}} \tag{1.11}$$

$$A\lambda^2 \equiv s_{23} = \lambda \left| \frac{V_{cb}}{V_{us}} \right| \tag{1.12}$$

$$A\lambda^3(\rho + i\eta) \equiv s_{13}e^{i\delta} = V_{ub}^* = \frac{A\lambda^3(\overline{\rho} + i\overline{\eta})\sqrt{1 - A^2\lambda^4}}{\sqrt{1-\lambda^2}[1 - A^2\lambda^4(\overline{\rho} + i\overline{\eta})]} \tag{1.13}$$

The vanishing combinations of the relations in equation 1.8 define triangles in the complex plane, of which there are six. The area of these traingles is of particular interest as a direct measure of the amount of CP-violation. Triangles of adjacent rows or columns of the CKM matrix possess a very short side and are almost degenerate, therefore the two relations:

$$V_{ud}V_{ub}^* + V_{cd}V_{cb}^* + V_{td}V_{tb}^* = 0 \tag{1.14}$$

$$V_{us}V_{ub}^* + V_{cs}V_{cb}^* + V_{ts}V_{tb}^* = 0 \tag{1.15}$$

are relevant to this discussion. The first one is the most commonly cited unitary relation which upon division by the most precisely defined value $V_{cd}V_{cb}^*$ yields a triangle in the complex plane shown in Fig. 1.1 with its vertices located at $(0,0)$, $(0,1)$ and $(\overline{\rho},\overline{\eta})$. The second of these relations that contains the s-quark mixing, can similarly be divided by $V_{cs}V_{cb}^*$ to yield an (almost degenerate) triangle with vertices at $(0,0)$, $(0,1)$ and $(\overline{\rho}_s,\overline{\eta}_s)$.

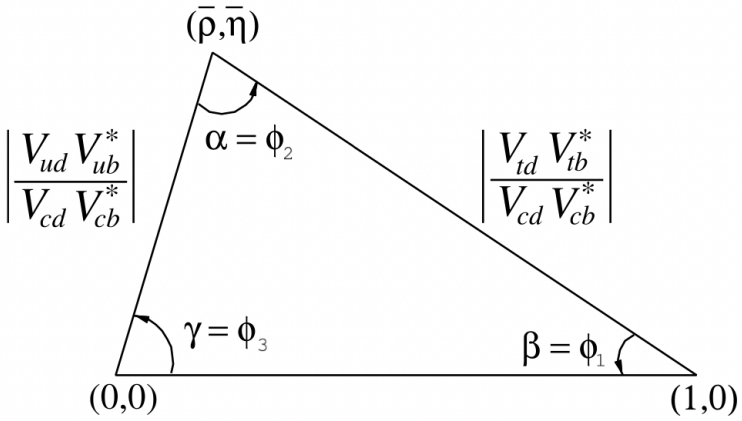

Figure 1.1: The unitary triangle

The different parameters that correspond to quark mixing have been measured in various experiments. The resultant $\alpha+\beta+\gamma = (179^{+7}_{-6})^\circ$ [3] is consistent with the Standard Model. Where angles of this triangle are defined as:

$$\begin{aligned}
\beta = \phi_2 &= \arg\left(-\frac{V_{cd}V_{cb}^*}{V_{td}V_{tb}^*}\right) \\
\alpha = \phi_2 &= \arg\left(-\frac{V_{td}V_{tb}^*}{V_{ud}V_{ub}^*}\right) \\
\gamma = \phi_2 &= \arg\left(-\frac{V_{ud}V_{ub}^*}{V_{cd}V_{cb}^*}\right)
\end{aligned} \tag{1.16}$$

Due to the involvement of CKM elements in CP-violation, the measurement of CP-violation phases can help constrain the values of the parameters $\overline{\rho}$ and $\overline{\eta}$. The best prescription for precise determination of CKM matrix elements is as reported by P. Z. et al. (Particle Data Group) [3] a global fit to all available measurement data with the imposition of the three generation unitarity constraint from the Standard Model. Mulltiple approaches exist for combining the experimental data. The CKMfitter grourp [4] & [5] uses frequentist statistics, while the UTfit group [6] and uses a Bayesian approach. Both approaches produce similar results. The values of the individual elements are laid out in Table 1.1

The unitarity constraints on the CKM matrix greatly reduce the allowed ranges of some of the CKM elements. The fit for the Wolfenstein parameters of equations 1.11 to 1.13 results in the following (constraints in Fig. 1.2 [4] & [5]):

$$\begin{aligned}
\lambda &= 0.22650 \pm 0.00048, \qquad A = 0.790^{+0.017}_{-0.012} \\
\overline{\rho} &= 0.141^{+0.016}_{-0.017}, \qquad \overline{\eta} = 0.357 \pm 0.011
\end{aligned} \tag{1.17}$$

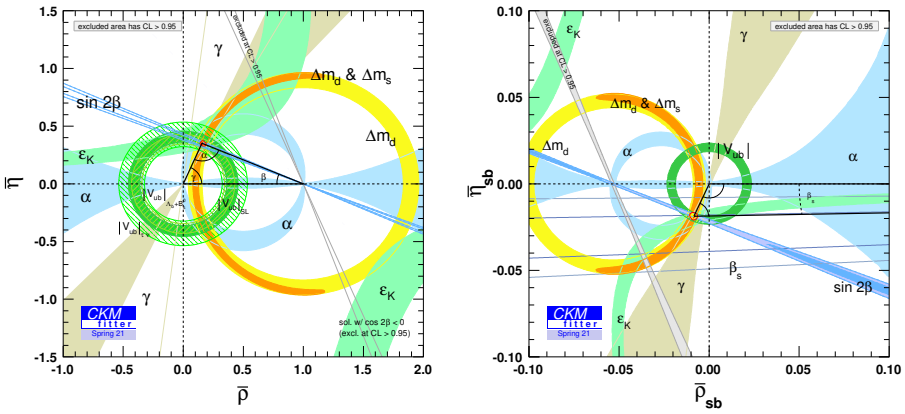

Figure 1.2: Constraints on the parameters $\overline{\rho}, \overline{\eta}$ (left) and $\overline{\rho}_{(s)}, \overline{\eta}_{(s)}$ (right) reported by the CKMFitter group. Shaded regions have $CL = 95\%$.

Table 1.1: The values of the CKM elements as per the result of the 2020 global fit. [2] The last column lists the commonly used measurement channels.

(Row,Col)	Element	Value	Channel
(1,1)	V_{ud}	0.97401 ± 0.00011	Nuclear β decays
(1,2)	V_{us}	0.22650 ± 0.00048	Semileptonic K decays
(1,3)	V_{ub}	$0.00361^{+0.00011}_{-0.00009}$	Semileptonic B decays
(2,1)	V_{cd}	0.22636 ± 0.00048	(Semi)leptopnic charm decays
(2,2)	V_{cs}	0.97320 ± 0.00011	Semileptonic D/Leptonic D_s decays
(2,3)	V_{cb}	$0.04053^{+0.00083}_{-0.00061}$	Semileptonic B to charm decays
(3,1)	V_{td}	$0.0085^{+0.00023}_{-0.00016}$	$B_d - \overline{B}_d$ mixing with $V_{tb} = 1$
(3,2)	V_{ts}	$0.03978^{+0.00082}_{-0.00060}$	$B_s - \overline{B}_s$ mixing with $V_{tb} = 1$
(3,3)	V_{tb}	$0.999172^{+0.000024}_{-0.000035}$	Single t-quark production

The degeneracy in the s-quark triangle is visible in Fig. 1.2. It is known since the measurements of γ and α that the Standard Model gives the leading contribution to $B^0 - \overline{B}^0$ mixing (Fig. 1.2 - B_s oscillation). Novel physics with a generic weak phase may nonetheless contribute to neutral meson mixings at a significant fraction of the Standard Model. A key parameter in the B_s system, the angle $\beta_s = \arg(-V_{ts}V_{tb}^*/V_{cs}V_{cb}^*)$, an angle of the flattened unitary triangle obtained by taking the scalar product of the second and third columns of the CKM matrix, can be measured via time-dependent CP-violation in $B_s \to J/\psi\phi$ decays, which are the focus of this study. The $J/\psi\phi$ state is not a CP eigenstate, therefore angular analysis of the final decay products is required to separate the CP-even and CP-odd components, which give opposite asymmetries [3].

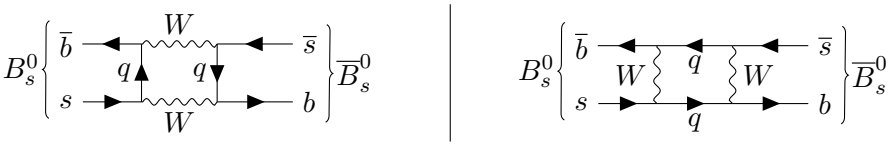

Figure 1.3: $B_s - \overline{B}_s$ oscillations

1.3 CP-violation and the B_s system

The phenomenon of CP-violation, discovered over 50 years ago, is central to the explanation of the observed dominance of matter over antimatter in the universe. As a consequence, it commands the interest of researchers [7]. In the Standard Model, CP-violation arises in the Yukawa sector through quark mixing, and is described by the phase δ in the CKM matrix. While the CKM phase accounts for observed CP-violating phenomena, it is notably not sufficient to explain the matter-antimatter imbalance in the universe. Thus a search for additional sources of CP-violation is strongly motivated.

The B_s^0 system in particular, is a great place to look for new physics based CP-violation effects. This is because the Standard Model predictions for several B_s^0 observables have good precision, and the Standard Model CP-violation is suppressed, making it more sensitive to new physics contributions. In particular, the angle β describing CP-violation in the B^0 system is of the order of 22° while the value of the corresponding β_s is of the order of 1°.

The quantum mechanical time evolution of some decaying particle $\mathcal{B}$ with mass $m_{\mathcal{B}}$ and decay width $\Gamma_{\mathcal{B}}$ (that is, lifetime $\tau_{\mathcal{B}} = 1/\Gamma_{\mathcal{B}}$) is given by:

$$|\mathcal{B}(t)\rangle = e^{-im_B t - \frac{\Gamma_B}{2}t} |\mathcal{B}(0)\rangle \tag{1.18}$$

If we now consider the flavour eigenstates of the B_s system, $|B_s\rangle = |\overline{b}s\rangle$ and $|\overline{B}_s\rangle = |b\overline{s}\rangle$, the time evolution can be described by the Schrödinger equation:

$$i\frac{d}{dt}\begin{pmatrix}|B_s(t)\rangle \\ |\overline{B}_s(t)\rangle\end{pmatrix} = \left(\hat{M} - \frac{i}{2}\hat{\Gamma}\right)\begin{pmatrix}|B_s(t)\rangle \\ |\overline{B}_s(t)\rangle\end{pmatrix} \tag{1.19}$$

While one may naïvely assume, the 2×2 hermitian matrices $\hat{M}$ and $\hat{\Gamma}$ to be diagonal matrices with elements simply equal to $m_{B_s^0}$ and $\Gamma_{B_s^0}$ respectively, the weak interaction based oscillations between the two flavour eigenstates through the box diagrams of Fig. 1.2 give rise to off diagonal elements. In general any combination of the flavour eigenstates of the form:

$$|\psi(0)\rangle = a(0)\,|B_s^0\rangle + b(0)\,|\overline{B}_s^0\rangle \tag{1.20}$$

would evolve in time by oscillating or decaying to any available final states

$$|\psi(t)\rangle = a(t)\,|B_s^0\rangle + b(t)\,|\overline{B}_s^0\rangle + c_1(t)\,|f_1\rangle + c_2(t)\,|f_2\rangle \ldots \tag{1.21}$$

Clearly, in the hamiltonian $\mathscr{H} = \hat{M} - \frac{i}{2}\hat{\Gamma}$ the diagonal entries are associated with flavour conserving transitions $B_s^0 \to B_s^0$ and $\overline{B}_s^0 \to \overline{B^0}_s$ while the off-diagonal entries are associated with flavour changing transitions $B_s^0 \to \overline{B}_s^0$ and $\overline{B}_s^0 \to B_s^0$. Now, in order to obtain physical eigenstates of the mesons, with definite mass and total decay width, the matrices $\hat{M}$ and $\hat{\Gamma}$ need to be diagonalised, resulting in the mass eigenstates $|B_{s,L}^0\rangle$ and $|B_{s,H}^0\rangle$, L=Light and H=Heavy:

$$\begin{aligned} |B_{s,L}^0\rangle &= p\,|B_s^0\rangle + q\,|\overline{B}_s^0\rangle \\ |B_{s,H}^0\rangle &= p\,|B_s^0\rangle - q\,|\overline{B}_s^0\rangle \end{aligned} \tag{1.22}$$

which are not generally orthogonal. Correspondingly, masses and decay rates m_H, m_L and Γ_H, Γ_L are associated to these states. The complex amplitudes satisfy the relation $|p|^2 + |q|^2 = 1$. The diagonalisation proceeds as follows [8]:

$$Q^{-1}\mathscr{H}Q = \begin{pmatrix} m_L - i\Gamma_L/2 & 0 \\ 0 & m_H - i\Gamma_H/2 \end{pmatrix} \tag{1.23}$$

$$Q = \begin{pmatrix} p & p \\ q & -q \end{pmatrix} \qquad Q^{-1} = \frac{1}{2pq}\begin{pmatrix} q & p \\ q & -p \end{pmatrix} \tag{1.24}$$

Considering that the mass eigenstates evolve by simple exponential decay as in 1.18. We can transform back to the flavour basis and write:

$$\begin{pmatrix} |B_s^0(t)\rangle \\ |\overline{B}_s^0(t)\rangle \end{pmatrix} = Q \begin{pmatrix} e^{-im_L t - \Gamma_L t/2} & 0 \\ 0 & e^{-im_H t - \Gamma_H t/2} \end{pmatrix} Q^{-1} \begin{pmatrix} |B_s^0(0)\rangle \\ |\overline{B}_s^0(0)\rangle \end{pmatrix} \tag{1.25}$$

The action of the CP operator is defined:

$$CP\,|B_s^0\rangle = -\,|\overline{B}_s^0\rangle \qquad CP\,|\overline{B}_s^0\rangle = -\,|B_s^0\rangle \tag{1.26}$$

resulting in the CP eigenstates

$$\begin{aligned} |B_s^{odd}\rangle &= \frac{1}{\sqrt{2}}\,|B_s^0\rangle + \frac{1}{\sqrt{2}}\,|\overline{B}_s^0\rangle \\ |B_s^{even}\rangle &= \frac{1}{\sqrt{2}}\,|B_s^0\rangle - \frac{1}{\sqrt{2}}\,|\overline{B}_s^0\rangle \end{aligned} \tag{1.27}$$

In the absence of CP-violation in the mixing, which is approximately the case in the SM, the heavy eigenstate is CP-odd and the light eigenstate is CP-even. This would be the case where $p = 1/\sqrt{2}$ and $q = -1/\sqrt{2}$. In practice we have:

$$|B^0_{s,H}\rangle \approx |B^{odd}_s\rangle \qquad |B^0_{s,L}\rangle \approx |B^{even}_s\rangle \tag{1.28}$$

We express the mass and width differences respectively as:

$$\Delta m_s \equiv m_H - m_L > 0 \qquad \Delta\Gamma_s \equiv \Gamma_H - \Gamma_L \tag{1.29}$$

On solving for the eigenvalues, the ratio q/p can be expressed as:

$$\frac{q}{p} = \sqrt{\frac{M^*_{12} - \frac{i}{2}\Gamma^*_{12}}{M_{12} - \frac{i}{2}\Gamma_{12}}} \tag{1.30}$$

Finally, one can express the matrix in 1.25 as:

$$Q \begin{pmatrix} e^{-im_L t - \Gamma_L t/2} & 0 \\ 0 & e^{-im_H t - \Gamma_H t/2} \end{pmatrix} Q^{-1} = \begin{pmatrix} g_+(t) & \frac{q}{p} g_-(t) \\ \frac{p}{q} g_-(t) & g_+(t) \end{pmatrix} \tag{1.31}$$

where

$$g_\pm = \frac{1}{2}\left(e^{-im_H t - \frac{1}{2}\Gamma_H t} \pm e^{-im_L t - \frac{1}{2}\Gamma_L t}\right) \tag{1.32}$$

Which implies, the solution of the Schrödinger equation for pure flavour eigenstates, expressing a transparent picture of $B_s - \overline{B}_s$ flavour oscillations, is then:

$$\begin{aligned} |B^0_s(t)\rangle &= g_+(t)\,|B^0_s(0)\rangle - \frac{q}{p} g_-(t)\,|\overline{B}^0_s(0)\rangle \\ |\overline{B}^0_s(t)\rangle &= g_+(t)\,|\overline{B}^0_s(0)\rangle - \frac{p}{q} g_-(t)\,|B^0_s(0)\rangle \end{aligned} \tag{1.33}$$

1.3.1 Classification of CP-violating effects

If we consider the decay of a neutral meson, M to some final state $|f\rangle$, the decay rate can be expressed as usual:

$$\Gamma_f \equiv \Gamma(M^0(t) \to f) = |\,\langle f|\,\mathscr{H}\,|M^0(t)\rangle\,|^2 \tag{1.34}$$

Three types of CP-violating effects can be distinguished in meson decays [7]:

1. CP-violation in decays
2. CP-violation in mixing
3. CP-violation in interference

CP-violation in decays or *direct CP-violation* arises when we have the amplitude for a meson (M) decaying to a final state f, $\mathcal{A}_f = \langle f | \mathscr{H} | M^0(t) \rangle$ differing from the amplitude of the decay of the CP-conjugate state to the final state $\overline{f}$, $\overline{\mathcal{A}}_{\overline{f}} = \langle \overline{f} | \mathscr{H} | \overline{M}^0(t) \rangle$, that is $|\overline{\mathcal{A}}_{\overline{f}}/\mathcal{A}_f| \neq 1$. For charged mesons, where mixing isn't a possibility, this is the only source of CP-violation. We can express the so called asymmetry as:

$$A_{\text{dirCP},f} = \frac{\Gamma(M^0(t) \to f) - \Gamma(\overline{M}^0(t) \to \overline{f})}{\Gamma(M^0(t) \to f) + \Gamma(\overline{M}^0(t) \to \overline{f})} = \frac{1 - |\frac{\overline{\mathcal{A}}_{\overline{f}}}{\mathcal{A}_f}|^2}{1 + |\frac{\overline{\mathcal{A}}_{\overline{f}}}{\mathcal{A}_f}|^2} \tag{1.35}$$

CP-violation in mixing, which relates only to neutral mesons, arises due to unequal proportions of the flavour eigenstates in the mass eigenstates $|q/p| \neq 1$. That is, the oscillation is favoured in one direction, $P(M \to \overline{M}) \neq P(\overline{M} \to M)$. This is measured via flavour-specific decays, that is, decays characterised by no direct CP-violation, and having vanishing cross flavour amplitudes, forbidding direct decays of the form $M \to \overline{f}$ and $\overline{M} \to f$, allowing these transitions to only occur through mixing as $\overline{M} \to M \to f$:

$$\mathcal{A}_{\overline{f}} = \langle \overline{f} | \mathscr{H} | M^0(t) \rangle = \mathcal{A}_f = \langle f | \mathscr{H} | \overline{M}^0(t) \rangle = 0 \tag{1.36}$$

The time-dependent asymmetry for this is expressed by:

$$A_{\text{mixCP},f} = \frac{\Gamma(M^0(t) \to \overline{f}) - \Gamma(\overline{M}^0(t) \to f)}{\Gamma(M^0(t) \to \overline{f}) + \Gamma(\overline{M}^0(t) \to f)} = \frac{1 - |\frac{q}{p}|^4}{1 + |\frac{q}{p}|^4} \tag{1.37}$$

Lastly, CP-violation in interference occurs when the same final state f is accessible to both M and $\overline{M}$, as is the case for the $J/\psi\phi$ final state for the B_s^0 and $\overline{B}_s^0$. It is a measure of the interference between the $M \to f$ and $M \to \overline{M} \to f$ reactions. It is characterised by a quantity:

$$\lambda_f = \frac{q}{p}\frac{\overline{\mathcal{A}}_f}{\mathcal{A}_f} \neq \pm 1 \tag{1.38}$$

This quantity is invariant under arbitrary re-phasing of the initial and final states, making it a potential observable in neutral meson decays. This type of CP-violation can occur even without individual mixing in either the decay or mixing with $\mathcal{I}m(\lambda_f) \neq 0$. The asymmetry is given by:

$$A_{\text{CP},f} = \frac{\Gamma(M^0(t) \to f) - \Gamma(\overline{M}^0(t) \to f)}{\Gamma(M^0(t) \to f) + \Gamma(\overline{M}^0(t) \to f)} \tag{1.39}$$

As reported in [7], this quantity can be calculated to be:

$$A_{\text{CP},f} \approx \frac{A_{\text{dirCP},f} \cos(\Delta m t) - A_{\text{mixCP},f} \sin(\Delta m t)}{1 + 2\frac{|\lambda_f|}{1+|\lambda_f|^2} \cos[\arg(\lambda_f)] \frac{\Delta\Gamma}{2\Gamma} \frac{t}{\tau} + \ldots} \tag{1.40}$$

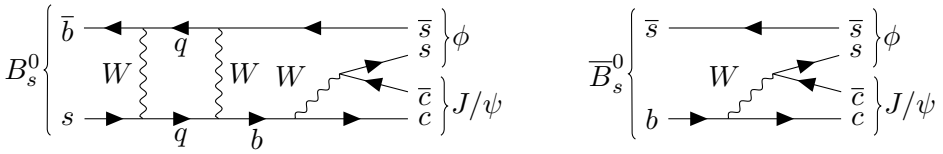

Figure 1.4: $B_s \to J/\psi\phi$ decays with and without mixing

1.4 Flavour Tagging

As established in the previous sections, the Cabibbo-Kobayashi-Maskawa mechanism enables the mixing between quark generations, and as a consequence the $B_s^0 - \overline{B}_s^0$ oscillations. Further, the measurement of the various parameters associated with the B_s^0, that is $\Delta\Gamma_s$, Δm_s, and the CP-violation phase $\phi_s = -2\beta_s$ can be measured by studying the $B_s^0 \to J/\psi\phi$ decay.

A key piece of information, that is essential to these measurements is the initial flavouring of the signal B_s^0, which is evidently complicated by the flavour oscillations. Several algorithms, called *taggers* are used to determine the initial $t = 0$ composition of the mesons. A tagger essentially relies on a systematically identified discriminating variable, say the charge of some decay product of the other b-object of the $b\overline{b}$ pair that contributed to the formation of the B_s^0, for example a lepton formed from a semileptonic decay, or a jet produced from the $b \to c \to s$ chain. The algorithm then produces a decision, d, about the flavouring. In practice, such an algorithm is characterised by a probability $P(b|d)$ of correct identification of flavour and the relative number of decay events it is able to tag. The per candidate $P_i(b|d)$ is an input to the maximum likelihood function used in a partial wave analysis fit described in section 3.3 that allows measurement of the parameters of interest.

In this study, an algorithm relying on the charge of kaons formed from the $s\overline{s}$ pair contributing to the B_s^0 is developed and studied to measure it's effectiveness, and the algorithm is deployed into the partial wave analysis program developed at ATLAS, CERN. The qualification of the algorithm and results of the fit are presented in the results sections 5.1 and 5.2.

Chapter 2

LHC & The ATLAS Experiment

In this chapter, a brief overview of the experimental setup, which generated the data used for this study is given. Section 2.1 goes over The LHC and particle acceleration, while section 2.2 is dedicated to a description of the ATLAS detector setup. b-hadron production is covered in section 2.4.

2.1 The Large Hadron Collider

The Large Hadron Collider (LHC) is the world's largest and and highest-energy particle accelerator, located outside of Geneva, Switzerland, beneath the Franco-Swiss border. Built by the *Conseil européen pour la recherche nucléaire* (CERN) in 2008, the accelerator consists of a 27 km ring of superconducting magnets, lying from 50 up to 175 m below the surface, in the tunnel which formerly housed the Large Electron-Positron Collider [9].

Several accelerating structures are used in succession (see 2.1) to attain an energy of 6.5 TeV per beam or a total collsion energy of $\sqrt{s} = 13$ TeV, which is the current world record. Initially, the Linear Particle Accelerator (LINAC 4) [10] generates 160 MeV negative hydrogen ions (H^-) which are injected into the Proton Synchroton Booster (PBS) where the electrons are stripped, leaving only the H^+ nuclei or single protons. From here, the protons are accelerated to 2 GeV and passed on to the Proton Synchrotron (PS) where they attain an energy of 26 GeV. The penultimate step is acceleration to 450 GeV, in the Super Proton Synchroton (SPS), after which the protons are injected into the main ring over 20 minutes as 2808 bunches of 115 billion protons each [11].

The main collider tunnel consists of two adjacent beamlines, where particles circulate in opposite directions, and intersect at 4 seperate collision points where the various experiments are located - the 4 major of which are ATLAS and CMS, for general-purpose detection and LHCb and ALICE for more specialised tasks, additionally four smaller experiments, TOTEM, MoEDAL, LHCf, and FASER are intended for highly specialised research. Interactions between bunches take place at discrete 25 ns intervals or at a collision frequency of 40 MHz.

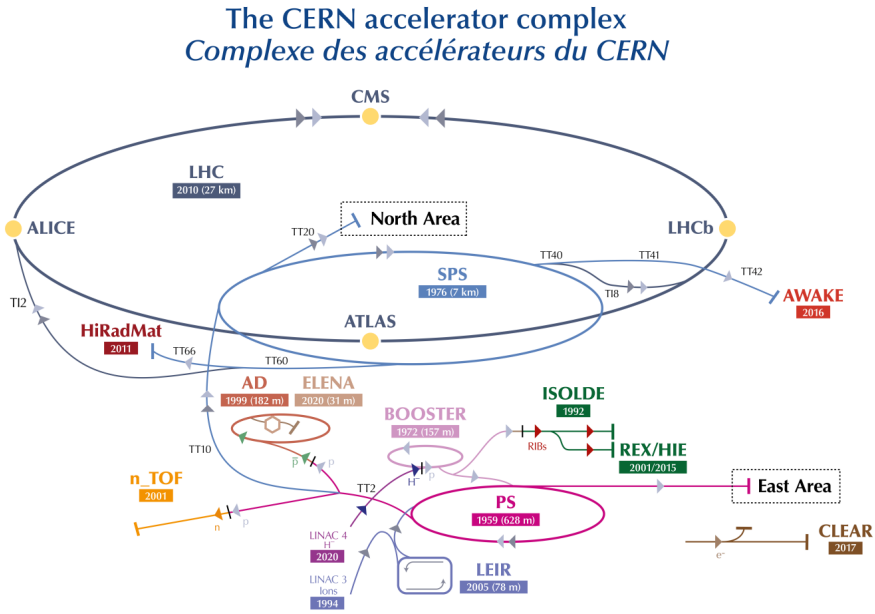

Figure 2.1: The Large Hadron Collider accelerator complex [12]

The LHC has a design luminosity (see section 2.3 of 10^{34} cm^{-2} s^{-1}, however twice this value was achieved by 2017. An array of 1,232 superconducting (NbTi cables maintained at 1.9 K by 5 cryogenic islands circulating superfluid helium) dipole electromagnets, 15 m in length and weighing 35 t with a design field strneght of 8.5 T over their length maintain the beam trajectory, while another 392 quadrupole magnets tasked with focusing the beam, especially near collision points, to maximise the probability of interaction.

The LHC is designed for 7 TeV beam energy or $\sqrt{s}$ =14 TeV. Data is generated at a rate of about 140 terabytes/day. Magnets of higher multipole orders are exploited to correct subtler imperfections in the field geometry. In total, about 10,000 superconducting magnets are installed.

In 2015 the LHC restarted after a two year break for upgrades following the first operational run lasting 2009-2013. While the electrical connectors of the magnets allowed operation at $\sqrt{s}$ =14 TeV, the bending magnets were only trained to handle $\sqrt{s}$ =13 TeV, which became the operating energy of Run-2 (2015-2018) which is the basis of this thesis. Another long shutdown (LS2) started in December, 2018. The whole CERN accelerator complex was maintained and upgraded to implement the High Luminosity Large Hadron Collider (HL-LHC) project that will increase the luminosity by a factor of 10. This shutdown ended in April, 2022. An overview of the operating values of the various parameters of the LHC can be found in Table 2.1. A standard cross section of the LHC dipoles is depicted in Fig. 2.2. Table 2.2 contains various Run-2 operating parameters.

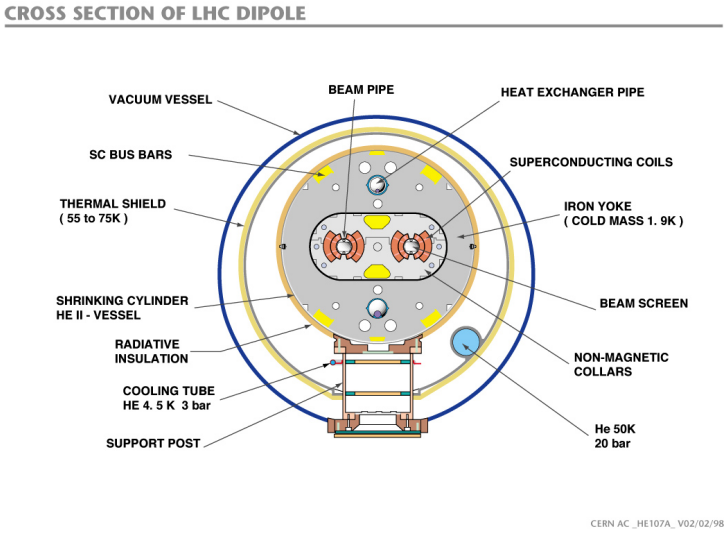

Figure 2.2: Standard cross-section of LHC dipole [13]

Table 2.1: Overview of operating parameters of The LHC [11]

Quantity	Number
Circumference	26,659 m
Dipole temperature	1.9 K
Number of magnets	9593
Number of main dipoles	1232
Number of main quadrupoles	392
Number of RF cavities	8/direction
Energy, protons	6.5 TeV
Peak magnetic dipole field	7.74 T
Luminosity	1.2×10^{34} cm^{-2} s^{-1}
Number of bunches/beam	2808
Number of protons/bunch	1.2×10^{11}

Table 2.2: Notable Run-2 conditions [14]

Property	2015	2016	2016	2017
Peak Luminosity ($\times 10^{34}$ cm^{-2} s^{-1})	0.5	1.38	2.09	2.14
Max. avg. collisions/bunch cross, $\mu_{\max}$	28.1	52.2	79.8	90.5
Max. colliding bunches	2232	2208	2544	2544

2.2 The ATLAS Experiment

A Toroidal **L**HC **A**pparatu**S** (ATLAS) [15] is the largest general-purpose particle detector experiment at the CERN designed to study massive particles. ATLAS is designed to study the broadest possible range of signals. This is so that any form that novel physical processes or particles might bear, the detector would be sensitive to it and its properties. ATLAS is designed to not only detect such particles, but also precisely measure parameters such as their masses (m), momenta (p), energies (E), lifetimes (τ), charges (q), and nuclear spins (s).

2.2.1 Coordinate System

The ATLAS experiment uses a right handed Cartesian coordinate system (x, y, z) to describe the detector and particle trajectories. The origin of the coordinate system lies on the nominal interaction point. The z-axis lies along the beamline, the x-axis points towards the centre of the circle, and the y-axis points upward. Additionally, a cylindrical coordinate system (r, ϕ, z) is defined. The radial distance $r = \sqrt{x^2 + y^2}$ measures the distance from the beam axis, the azimuthal angle $\phi = \arctan(y/x)$ is measured from the x-axis around the beam. A polar angle $\theta = \arctan(r/z)$ is also defined, usually represented by the pseudorapidity $\eta = -\ln\tan(\theta/2)$. The distance ΔR in azimuthal angle and pseudorapidity $\eta - \phi$ space is defined by $\Delta R = \sqrt{\Delta\phi^2 + \Delta\eta^2}$. The trajectory curvature is used to determine the transverse momentum of the particles, p_T.

2.2.2 Structure

The ATLAS detector, shown in Fig. 2.3 is a cylinder, with dimensions 46m length, 25m diameter, and sits in a cavern 100 m underground. The detector weighs a total of 7,000 tonnes. It is designed in a layered structure, with different types of detectors at different concentric stages, designed to record specific species of particles, such that all particles created at the central collision point can be characterised. The traces that particles leave in each separate layer of the detector enable reliable particle identification and accurate probing of energy and momentum. With an increase in the energy of the produced particles, a corresponding increase detector size is necessary to effectively measure and stop higher-energy particles. The stages of the detector can be divided into:

1. **The Inner Detector** (ID) begins a few centimetres from the beam axis, and extends to 1.2 m radially. It has a length of 6.2 m along the beam axis. It tracks particles through their interactions with the detector material at discrete points, it can ascertain the type of particle and measure kinematic parameters. The ID covers pseudorapidity range of $|\eta| < 2.5$. Nominal momentum measurements are for particles with $p_T > 0.5$ GeV, measured

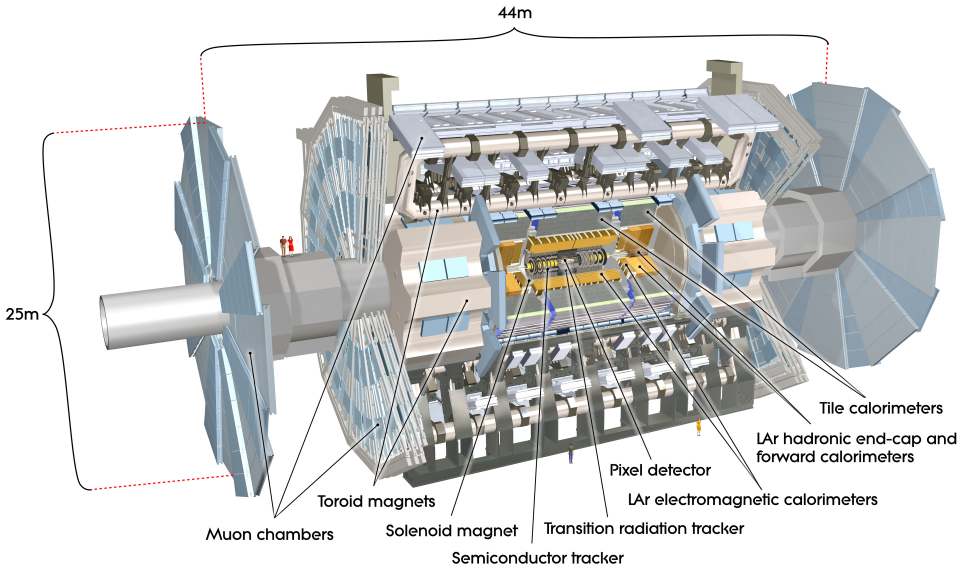

Figure 2.3: Schematic representation of the ATLAS detector [16].

with a resolution of $\sigma_{p_T}/p_T = 0.05\% \oplus 1\%$. The tracking precision enables measurements of primary and secondary vertex positions which are used for b-jet and τ-lepton tagging. The ID lies in a 2 T axial magnetic field generated by the superconducting solenoid magnet. It consists of three parts with different technologies [15]:

- The Pixel Detector, lying closest to the beam, is composed of four concentric layers and three disks on each end-cap. The three outer layers lie at 50.5 mm, 88.5 mm and 122.5 mm radially from the beam-line. The fourth innermost layer, Insertable B-Layer (IBL), is located at 33.25 mm. It was installed during Long Shutdown 1 before Run 2 of the LHC. Pixel is a cylinder, 1.4 m long with a 0.25 m radius and contains (excluding the IBL) 1,744 modules in total with dimensions 2 cm $\times$ 6 cm. The working material is is a 250 μm silicon layer. The smallest unit, *a pixel* that can be read measures 50 $\times$ 400 μm, and there are 47,000 of these. For the pixels in the barrel layers high intrinsic accuracies of 10 μm in $r-\phi$ coordinates and 115 μm in z are achieved. In the end-cap discs the intrinsic accuracies are 10 μm in $r-\phi$ and 115 μm in r.
- The Semi-Conduction Tracker (SCT) is the middle component of the inner detector. It is conceptually and functionally similar to the Pixel Detector but with four barrel layers composed of 4088 long, narrow two-sided silicon microstrips. Each strip measures 80 μm $\times$ 12 cm.

The SCT is tasked with basic tracking in the plane orthogonal to the beam. It has 6.3 million readout channels and a total area of 61 m^2. The intrinsic accuracies for modules in the barrel are 17 μm in $r - \phi$ and 580 μm in z coordinates. In the end-cap discs they are 17 μm in $r - \phi$ and 580 μm in r coordinates.

- The Transition Radiation Tracker is the outermost part of the ID, composed of about 50,000, 144 cm length and 4 mm diameter drift tubes (straws) aligned parallel to the beam pipe and about 250,000, 34 cm long straws in the end caps. The straws are filled with a mixture of Xe, CO_2 and O_2, and helt at -1,500 V. The drift tubes each bear a 31 μm diameter gold-plated tungsten wire, running through their centre. The wires that carry signals caused by ionization in the tubes create a pattern of 'hit' straws that allow the particle trajectory to be mapped, with an accuracy of 130 μm in $r - \phi$.

2. **The Calorimeters** sit outside the magnet surrounding the ID. Their purpose is energy measurement through absorption [17, 18]. They and are composed of two broad calorimeter systems:

   - The Electromagnetic (EM) Calorimeter, that absorbs energy from electromagnetically interacting particles. It is based on a liquid Argon (LAr) active material with a lead (Pb) absorber. It covers a range of $|\eta| < 3.2$. The relative energy resolution of the LAr calorimeter is parameterised by $\sigma_E/E = 10\%/\sqrt{E} \oplus 0.17/E \oplus 0.7\%$ in GeV.
   - The Hadronic Calorimeter, that surrounds the EM calorimeter and absorbs particles that pass through to it with $|\eta| < 3.2$, and interact via the strong force. The Hadron Calorimeter is based on two technologies: an LAr active material with copper absorbers, and plastic scintillator tiles 8 m in diameter and 12 m along the axis active material with a steel absorber. The relative energy resolution of the LAr and Tile calorimeters is $\sigma_E/E = 50\%/\sqrt{E} \oplus 3\%$. There are also forward calorimeters covering $3.1 < |\eta| < 4.9$.

3. **The Muon Spectrometer** (MS) lies from 4.5 m to the end of the detector at 11 m [19]. It is the outermost layer of ATLAS. It was built to measure the momentum of 100 GeV muons with 3% accuracy and of 1 TeV muons with 10%. Range covered is $|\eta| < 2.5$. It consists of three components:

   - Three toroidal magnets
   - 1200 high-precision tracking chambers
   - A set of trigger chambers

   It has about 10^6 readout channels, and its detectors have a total area of 12,000 m^2. It serves essentially to identify muons, which are for the most

part the only particles making it this far out. The chambers are aligned with a precision of 30-60 μm.

4. **The Magnet System** is composed of two subsystems that bend the particles' trajectories in order to measure the relativistic momentum of the particles. These systems are:

   - The solenoid magnet, which produces a 2 T magnetic field surrounding the ID. For the most part only particles with $p_T > 400$ MeV will make it out and be registered.
   - The toroid magnets, a set of eight large air-core superconducting barrel loops and two smaller end-cap air toroidal magnets, produce a 26 m long and 20 m diameter magnetic field of 2-8 T·m.

2.2.3 Trigger and Data Acquisition System (TDAQ)

As mentioned earlier, the beam collision rate of 40 MHz, combined with the average data size of an event of 1.5 Mb, mandates a close-to-real-time online decision about whether to store an event, so as to reduce the data load and select interesting events. This task is performed by the ATLAS trigger and data acquisition (TDAQ) system. A simplified schematic of this system is presented in Fig. 2.4 A reasonable storage rate within the current technical constraints is 1 KHz. A two-stage architecture is used to accomplish this:

1. **The Level 1 (L1) Trigger** employs dedicated hardware (Field Programmable Gate Arrays (FPGAs) and application-specific integrated circuit (ASICs) primarily) to run simple filtering algorithms to reduce the rate from 40 MHz to 100 KHz [20]. The L1 decision is made by the central trigger processor (CTP), on the basis of three inputs:

   - The L1-Calo, which receives low granularity information from the EM and hadronic calorimeters to identify high p_T electrons, photos, tau leptons, jets and missing transverse momentum (E_T^{miss}) events.
   - The L1-Muon, which uses resistive plate chambers (RPC) and thin gap chambers (TGC) to select muon candidates.
   - The L1-Topo performs topological selections on L1 objects, for example finding dielectron candidates with some minimum ΔR.

   If any of these triggers selects and event an L1-accept bit is set and the data from the detector is accessed, alongside identified regions of interest (ROI), and passed on to the High-Level Trigger (HLT). The L1 decision takes < 2.5 μs.

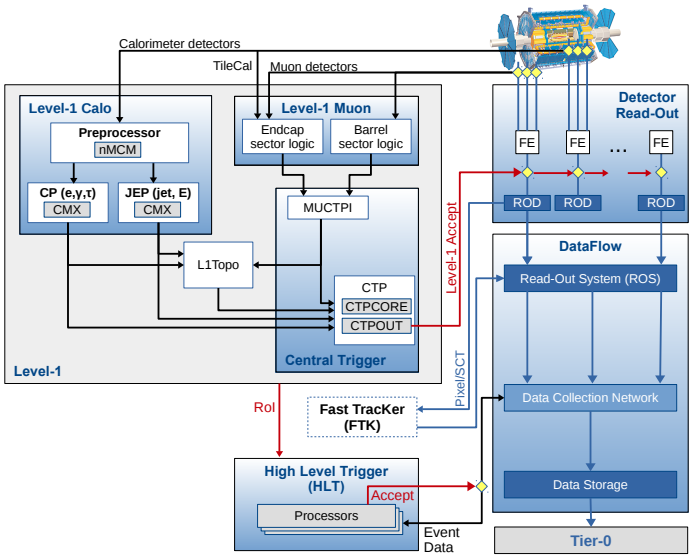

Figure 2.4: Schematic of the ATLAS TDAQ during Run-2 [21].

2. **The High-Level Trigger (HLT)** is executed on a nearby remote computing farm. It receives the L1-accept bits and ROIs and cuts the rate from 100 KHz to 1 KHz. The HLT is made of chains, each of which is series of feature extraction (FEX) and hypothesis algorithms, where the FEX algorithms perform additional calculation and the hypothesis algorithms give a pass/fail decision. If at least one chain passes, the data is stored at Tier-0. The time to process an event at HLT is 0.3 s.

This concludes the very brief overview of the LHC and ATLAS experiment. There are a lot of additional finer details, deemed to be out of the scope of this thesis and not explicitly mentioned, however they may be found by referring to the various sources cited over the previous sections.

Finally, after a few words on luminosity in the next section, we discuss the mechanism of b-hadron production at the LHC. The leading order diagrams are shown in Fig. 2.3.

Table 2.3: Summary of ATLAS detector subsystems

Subsystem	Component	Length [m]	Radius [m]	$\|\eta\|$ range
Inner Detector	Barrel	3.5	1.2	$\|\eta\| < 2.5$
EM Calorimeter	Barrel	2.8	1.4-2.0	$\|\eta\| < 2.5$
	End cap	0.3	2.1	$1.4 < \|\eta\| < 3.2$
Tile Calorimeter	Barrel	5.8	2.3-4.3	$\|\eta\| < 1.7$
	Extended Barrel	2.6	2.3-4.3	$\|\eta\| < 1.7$
Hadronic End Cap	-	1.8	2.0	$1.5 < \|\eta\| < 3.2$
Forward Calorimeter	-	1.3	0.5	$3.1 < \|\eta\| < 4.9$

2.3 Luminosity

Luminosity, the ratio of detected events over some time period divided by the corresponding cross section $\mathcal{L} = \frac{1}{\sigma}\frac{dN}{dt}$, is vital in estimating the number of signal and background events registered in the detector. Details can be found in [22]. The absolute luminosity may be calculated from the beam parameters as:

$$\mathcal{L}_b = \frac{f_{\text{rev}} n_1 n_2 n_b}{4\pi\sigma_x\sigma_y} \text{ cm}^{-2} \text{ s}^{-1} \tag{2.1}$$

where, f_{rev} is the beam revolution frequency, σ_x and σ_y are convolved beam sizes, n_1 and n_2 the number of protons in the colliding bunches and n_b the number of bunches.

The integrated luminosity is expressed as:

$$L = \int \mathcal{L} dt \tag{2.2}$$

over the entire data taking time periods. In ATLAS, the basic time unit of storing $\mathcal{L}$ is called a luminosity block (LB), over which conditions do not significantly vary and are assumed constant (≈ 1 minute).

Instantaneous luminosity measured is averaged over the luminosity block and stored. The integrated luminosity for an LB is calculated by multiplying instantaneous luminosity by the size of the LB. The integrated luminosity for a particular study a sum over the LBs of the given analysis. The integrated luminosity studied in this work is 139 fb^{-1}.

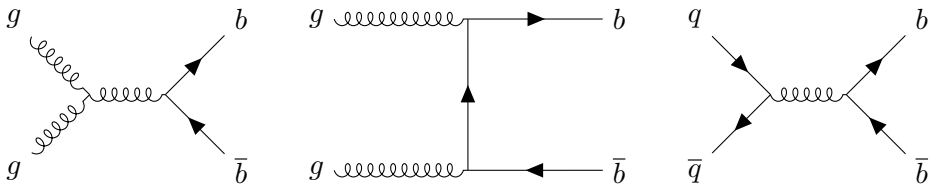

Figure 2.5: Leading order $\mathcal{O}(\alpha_s^2)$ diagrams for $b\bar{b}$ pair production at the LHC, crossing-symmetry variations are omitted for conciseness.

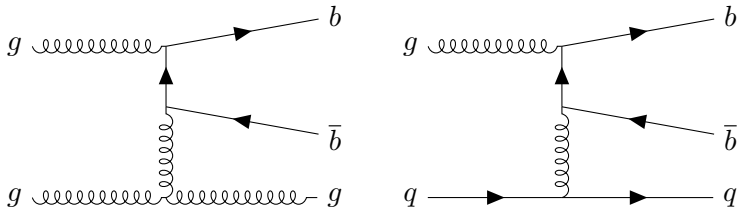

Figure 2.6: Next-to-leading order $\mathcal{O}(\alpha_s^3)$ diagrams for $b\bar{b}$ pair production through flavour excitation, crossing-symmetry variations are omitted for conciseness.

2.4 b-hadron production at the LHC

As opposed to the simple $e^+e^- \to Z \to b\bar{b}$ production channel of electron-position colliders, such as the LEP that preceded the LHC, the production of b-hadrons at the LHC in pp collisions takes place through flavour creation (leading order in α_s[1]), flavour excitation or gluon splitting (next-to-leading order in α_s). At the LHC the next-to-leading order flavour excitation processes are dominant as evidenced by the cross-section in Fig. 2.8, followed by the leading order pair creation and then gluon splitting.

Flavour creation or pair creation is sub-divided into gluon fusion $gg \to b\bar{b}$ and light quark annihilation $q\bar{q} \to b\bar{b}$, with the former being the more dominant one (it is described by the first two diagrams in Fig. 2.3, as well as a crossed version of the second diagram). These channels produce to back-to-back, well separated b-jets in the detector. Flavour excitation is the process, where a parton of one of the protons scatters off a sea b-quark in the in the other proton, exciting it into the final state. One of the b-quark undergoes a hard QCD interaction, and the other would proceed with then initial proton undetected. Gluon splitting refers to the processes in which the pair arises from a $g \to b\bar{b}$ splitting in the initial or final state. This is overall a soft process producing the quarks very close in phase, such that their decay products may appear to have a common parent.

[1] $\alpha_s(p^2) = g_s^2(p^2)/4\pi$

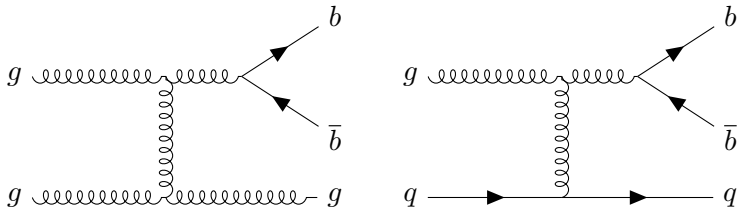

Figure 2.7: Next-to-leading order $\mathcal{O}(\alpha_s^3)$ diagrams for $b\bar{b}$ pair production through gluon splitting

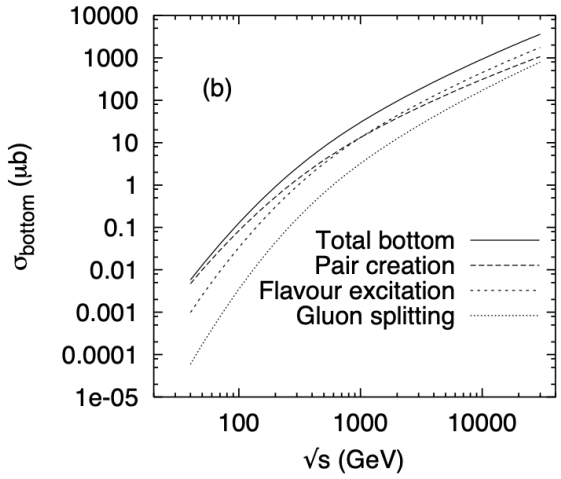

Figure 2.8: The total bottom cross sections for pp collisions as a function of $E_{CM} = \sqrt{s}$. The contributions from pair creation, flavor excitation and gluon splitting are shown separately

The quarks in the $b\bar{b}$ pair then fragmentise into hadrons. The probability to fragmentise into a B_s is given by [3]

$$B(\bar{b} \to B_s) = 10.0 \pm 0.8\% \tag{2.3}$$

and the full branching of the $B_s \to J/\psi\phi \to \mu^+\mu^- K^+ K^-$ decay:

$$\begin{aligned} \mathcal{B}(B_s \to J/\psi\phi) &= (1.08 \pm 0.08) \times 10^{-3} \\ \mathcal{B}(J/\psi \to \mu^+\mu^-) &= (5.961 \pm 0.033)\% \\ \mathcal{B}(\phi \to K^+K^-) &= (49.2 \pm 0.5)\% \end{aligned} \tag{2.4}$$

Chapter 3

Study of the decay $B_s^0 \to J/\psi(\to \mu^+\mu^-)\phi(\to K^+K^-)$

As was mentioned in section 1.3 the B_s^0 system, and in particular the $B_s^0 \to J/\psi(\to \mu^+\mu^-)\phi(\to K^+K^-)$ decay, is an attractive channel for study – allowing access to an interesting observable, sensitive to new physics. The combined branching fraction of $\mathcal{B}_{\text{comb}} \sim 10^{-5}$ as reported in section 2.4 allows the collection of significant samples, and the charged final products, allow for good reconstruction. This chapter is dedicated to discussing the angular distribution, mentioned in section 1.2 of the decay rate and the data ntuple analysed in section 3.1, reconstruction and selection in section 3.2 and explaining the various parameters and partial wave analysis fit strategy used to measure them in section 3.3.

3.1 Differential Decay Rate and Helicity Amplitudes

In section 1.3, it was mentioned that in the SM, we have $|p/q| \approx 1$, meaning that $|B^0_{s,H}\rangle$ is nearly CP-odd and $|B^0_{s,L}\rangle$ is nearly CP-even. The final state $J/\psi\phi$ is composed of both CP-odd and CP-even states. Since the B_s^0 is a pseudoscalar ($J^P = 0^-$)[1] and the J/ψ and ϕ are both vector particles ($J^{PC} = 1^{--}$), the decay products can have the orbital angular momentum, $L = 0, 1, 2$. Correspondingly three amplitudes A_0 ($L = 0$, CP-even, longitudinally polarised) $A_\perp$ ($L = 1$, CP-odd, transversely polarised) and $A_{||}$ ($L = 2$, CP-even, transversely polarised) characterise the decay. Here 'longitudinal' and 'transverse' are with respect to the decay axis. Fig. 3.1 depicts the transversity angles (θ_T, ϕ_T and ψ_T), while Table 3.1 and the subsequent equations lay out the functions, used in defining the temporal and angular distribution given by differential decay rate [23]:

$$\frac{d^4\Gamma}{dtd\Omega} = \sum_{k=1}^{10} \mathscr{O}^{(k)}(t) g^{(k)}(\theta_T, \psi_T, \phi_T) \tag{3.1}$$

[1] Here J represents angular momentum and the superscript the parity

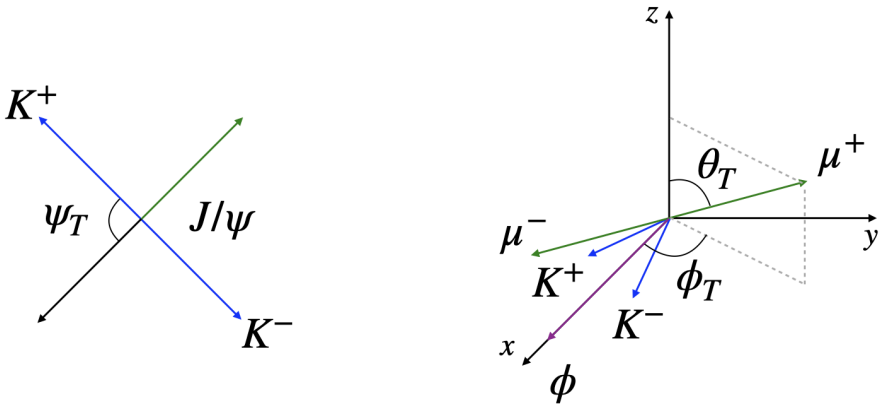

Figure 3.1: Definition of the transversity angles. Note, ψ_T is measured in the rest frame of the ϕ, while θ_T and ψ_T are measured in the rest frame of the J/ψ

Table 3.1: The angular functions of the decay rate and the time independent components of the $\mathscr{O}^{(k)}$, which can be split into $\mathscr{O}^{(k)}(t) = A^{(k)}(0)T^{(k)}(t)$

k	$g^{(k)}(\theta_T, \psi_T, \phi_T)$	$A^{(k)}(0)$
1	$2\cos^2\psi_T(1-\sin^2\theta_T\cos^2\phi_T)$	$\frac{1}{2}\lvert A_0(0)\rvert^2$
2	$\sin^2\psi_T(1-\sin^2\theta_T\sin^2\phi_T)$	$\frac{1}{2}\lvert A_{\lvert\rvert}(0)\rvert^2$
3	$\frac{1}{\sqrt{2}}\sin 2\psi_T\sin^2\theta_T\sin 2\phi_T$	$\frac{1}{2}\lvert A_0(0)\rvert\lvert A_{\lvert\rvert}(0)\rvert\cos\delta_{\lvert\rvert}$
4	$\sin^2\psi_T\sin^2\theta_T$	$\frac{1}{2}\lvert A_\perp(0)\rvert^2$
5	$\frac{2}{3}(1-\sin^2\theta_T\cos^2\phi_T)$	$\frac{1}{2}\lvert A_S(0)\rvert^2$
6	$\frac{1}{3}\sqrt{6}\sin\psi_T\sin 2\theta_T\cos\phi_T$	$\frac{1}{2}\alpha\lvert A_S(0)\rvert\lvert A_\perp(0)\rvert\sin(\delta_\perp-\delta_S)$
7	$-\sin^2\psi_T\sin 2\theta_T\sin\phi_T$	$\frac{1}{2}\lvert A_{\lvert\rvert}(0)\rvert\lvert A_\perp(0)\rvert$
8	$\frac{1}{\sqrt{2}}\sin 2\psi_T\sin 2\theta_T\cos\phi_T$	$\frac{1}{2}\lvert A_0(0)\rvert\lvert A_\perp(0)\rvert$
9	$\frac{1}{3}\sqrt{6}\sin\psi_T\sin^2\theta_T\sin 2\phi_T$	$\frac{1}{2}\alpha\lvert A_S(0)\rvert\lvert A_{\lvert\rvert}(0)\rvert$
10	$\frac{4}{3}\sqrt{3}\cos\psi_T(1-\sin^2\theta_T\cos^2\phi_T)$	$\frac{1}{2}\alpha\lvert A_0(0)\rvert\lvert A_S(0)\rvert$

Additionally, we have:

$$\begin{aligned}
\delta_7 &= \delta_\perp - \delta_{||} \\
\delta_9 &= \frac{\pi}{2} - (\delta_{||} - \delta_S) \\
\delta_8 &= \delta_\perp \\
\delta_{10} &= \frac{\pi}{2} + \delta_S
\end{aligned} \tag{3.2}$$

Which fit into the time-evolution components $T^{(k)}$ given by:

$$
\begin{aligned}
T^{(1,2,3)} &= \left(1 + \frac{2|\lambda|}{1+|\lambda|^2}\cos\phi_s\right) e^{-\Gamma_{s,L}t} + \left(1 - \frac{2|\lambda|}{1+|\lambda|^2}\cos\phi_s\right) e^{-\Gamma_{s,H}t} \\
&\quad \pm 2e^{-\Gamma_s t}\left(\frac{2|\lambda|}{1+|\lambda|^2}\sin(\Delta m_s t)\sin\phi_s + \frac{1-|\lambda|^2}{1+|\lambda|^2}\cos(\Delta m_s t)\right) \\
T^{(4,5,6)} &= \left(1 - \frac{2|\lambda|}{1+|\lambda|^2}\cos\phi_s\right) e^{-\Gamma_{s,L}t} + \left(1 + \frac{2|\lambda|}{1+|\lambda|^2}\cos\phi_s\right) e^{-\Gamma_{s,H}t} \\
&\quad \mp 2e^{-\Gamma_s t}\left(\frac{2|\lambda|}{1+|\lambda|^2}\sin(\Delta m_s t)\sin\phi_s - \frac{1-|\lambda|^2}{1+|\lambda|^2}\cos(\Delta m_s t)\right) \qquad (3.3) \\
T^{(7-10)} &= \left(e^{-\Gamma_{s,L}t} - e^{-\Gamma_{s,H}t}\right)\frac{2|\lambda|}{1+|\lambda|^2}\cos\delta_k\sin\phi_s \\
&\quad + \frac{1}{2}\left(e^{-\Gamma_{s,L}t} + e^{-\Gamma_{s,H}t}\right)\frac{1-|\lambda|^2}{1+|\lambda|^2}\sin\delta_k \\
&\quad \pm 2e^{\Gamma_s t}\left(\sin\delta_k\cos(\Delta m_s t) - \frac{2|\lambda|}{1+|\lambda|^2}\cos\delta_k\cos\phi_s\sin(\Delta m_s t)\right)
\end{aligned}
$$

The time-dependent functions $\mathscr{O}^{(k)}$ are split into $\mathscr{O}^{(k)}(t) = A^{(k)}(0)T^{(k)}(t)$ where the $T^{(k)}(t)$[2] contain the time evolution. The amplitude A_S accounts for the contribution from the non-resonant $B_s^0 \to J/\psi f_0(980)(\to K^+K^-)$ channel with the spin-0 $f_0(980)$ or K^+K^- states. The amplitudes are parameterised as $|A_j|e^{i\delta_j}$, with $j = \{0, ||, \perp, S\}$ and $\delta_0 = 0$[3]. The normalisation condition is:

$$|A_0(0)|^2 + |A_\perp(0)|^2 + |A_{||}(0)|^2 = 1 \qquad (3.4)$$

The quantity $|A_S|^2$ is the ratio of non-resonant to resonant yield in the chosen mass interval. The strong phase δ_S is the phase difference between A_0 and A_S at the K^+K^- resonance peak. In the sum over the mass interval, the interference terms are corrected by a factor $\alpha = 0.51 \pm 0.02$, based on the Breit-Wigner characterisation of the resonance, assuming a uniform A_S, that accounts for the mass-dependent differences in absolute amplitude and phase between the resonant and S-wave amplitudes. The uncertainty is calculated by the Flatté parameterisation [24]. At the places where either $\pm$ or $\mp$ is used, the upper (lower) sign describes the decay of an initial B_s^0 ($\overline{B}_s^0$) meson.

Analytical projections of the differential decay rate onto the angular axes can be seen in Fig. 3.2 (shown for comparison). Subsequently, the angular distributions of the data ntuple analysed are shown in Fig. 3.3.

[2]The 'f' subscript in λ_f is dropped for simplicity.
[3]By convention

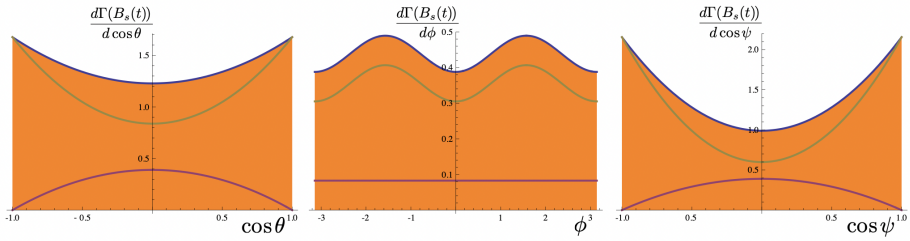

Figure 3.2: Projections of $d^4\Gamma/dtd\Omega$ onto the angular axes. The CP-even and CP-odd contributions are indicated by the green and pink line respectively [25].

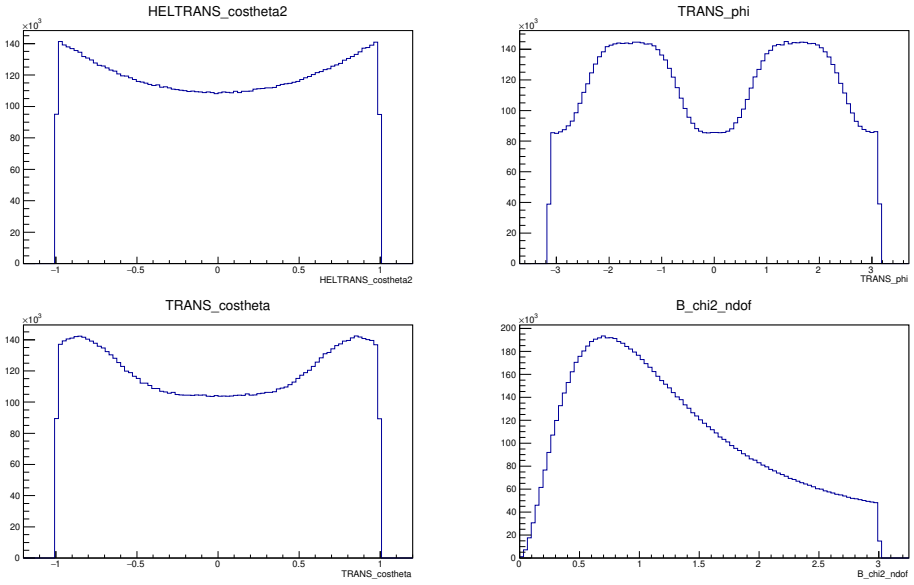

Figure 3.3: Distribution of analysed events along the $\cos\theta_T$ (top left), ϕ_T (top right) and $\cos\psi_T$ (bottom left) angular axes and over χ^2/N_{dof} (bottom right).

The transversity angles θ_T, ϕ_T and ψ_T are defined as:

- θ_T is the angle between the 3-momentum of the antimuon $\vec{p}(\mu^+)$ and the normal to the $x-y$ plane in the rest frame of the J/ψ.
- ϕ_T is the angle between the projection of $\vec{p}(\mu^+)$ onto the $x-y$ plane, and the x-axis in the rest frame of the J/ψ.
- ψ_T is the angle between the reversed 3-momentum of the J/ψ, $-\vec{p}(J/\psi)$ and the 3-momentum vector of the positively charged kaon $\vec{p}(K^+)$ in the rest frame of the ϕ.

3.2 Reconstruction and Event Selection

Candidates containing the $B_s^0 \to J/\psi(\to \mu^+\mu^-)\phi(\to K^+K^-)$ decay of study are required to undergo following the reconstruction and selection procedure [26]:

1. The candidate must pass the initial trigger selections.
2. One reconstructed *primary vertex* and at least one pair of oppositely charged $\mu^+\mu^-$ candidates must be present.
3. Four ID tracks must contribute to the formation of said primary vertex.
4. Muon candidates, reconstructed by both the ID and MS, are classified into *tight* and *low* p_T GeV using the ID measurement (See section 4.3.2).
5. Muon pairs are re-fitted to a common vertex, and accepted if the quality satisties $\chi^2/N_{\text{dof}} < 10$.
6. Due to considerations of varying mass resolution over different sections of the detector, the J/ψ candidates are classified into three regions. The signal region is defined such that 99.7% of the J/ψ candidates are retained. The mass resolutions are obtained through maximum likelihood fits. The regions are defined as follows:
   - Both muons have pseudorapidity $|\eta| < 1.05$. The extreme values correspond to the edges of the MS barrel.
   - One muon has $1.05 < |\eta| < 2.5$ and the other $|\eta| < 1.05$.
   - Both muons have $1.05 < |\eta| < 2.5$.
7. Pairs of oppositely charged tracks, not identified as muons or electrons and having $p_T > 1$ GeV and $|\eta| < 2.5$ are used to reconstruct $\phi \to K^+K^-$ candidates.
8. Tracks for each combination of $J/\psi \to \mu^+\mu^-$ and $\phi \to K^+K^-$ that are fitted to a common vertex with the J/ψ mass fixed to the invariant mass of the muon pair and the ϕ mass, based on the invariant mass of the K^+K^- lying in the 1.0085 GeV $< m(K^+K^-) <$ 1.0305 GeV interval are selected as $B_s^0 \to J/\psi(\to \mu^+\mu^-)\phi(\to K^+K^-)$ candidates.
9. A track quadruplet, having passed the above criteria, is selected for further analysis if the vertex fit quality satisfies $\chi^2/N_{\text{dof}} < 3$ (See 3.3). The lowest χ^2/N_{dof} candidate is chosen if multiple candidates pass the selection for an event.
10. The best candidate for the primary vertex is chosen as the candidate with the smallest 3D impact parameter a_0, the minimum distance between each primary vertex candidate and the line extrapolated from the reconstructed B_s^0 meson candidate vertex in the direction of the B_s^0 momentum.

3.3 Maximum Likelihood Fit

The events that pass the selection described in the previous section are then stored for offline analysis. For extraction of the parameter values of the $B_s^0 \to J/\psi(\to \mu^+\mu^-)\phi(\to K^+K^-)$ decay, an unbinned maximum likelihood fit is performed. The likelihood function used is defined as follows (See Table 3.2) [26]:

$$\begin{aligned}\ln \mathscr{L} = \sum_{i=1}^{N} w_i \cdot \ln[& f_s \cdot \mathcal{F}_s(m_i, \tau_i, \sigma_{m_i}, \sigma_{\tau_i}, \Omega_i, P_i(B|Q_x), p_{T_i}) \\ & + f_s \cdot f_{B^0} \cdot \mathcal{F}_{B^0}(m_i, \tau_i, \sigma_{m_i}, \sigma_{\tau_i}, \Omega_i, P_i(B|Q_x), p_{T_i}) \\ & + f_s \cdot f_{\Lambda_b} \cdot \mathcal{F}_{\Lambda_b}(m_i, \tau_i, \sigma_{m_i}, \sigma_{\tau_i}, \Omega_i, P_i(B|Q_x), p_{T_i}) \\ & + (1 - f_s \cdot (1 + f_{B^0} + f_{\Lambda_b})) \cdot \mathcal{F}_{\text{bkg}}(m_i, \tau_i, \sigma_{m_i}, \sigma_{\tau_i}, \Omega_i, P_i(B|Q_x), p_{T_i})]\end{aligned} \tag{3.5}$$

Table 3.2: Summary of maximum likelihood function parameters

Parameter	Description
N	Number of selected candidates
w_i	Weighting factor accounting for trigger efficiency
f_s	Fraction of signal candidates
$\mathcal{F}_s$	Signal probability distribution function (See 3.3.1)
f_{B^0}	Fraction of misidentified B^0 background
$\mathcal{F}_{B^0}$	B^0 background probability distribution function
f_{Λ_b}	Fraction of misidentified Λ_b baryon background
$\mathcal{F}_{\Lambda_b}$	Λ_b baryon background probability distribution function
$\mathcal{F}_{\text{bkg}}$	'Other' background probability distribution function
m_i	Reconstructed mass
σ_{m_i}	Error in reconstructed mass
τ_i	Proper decay time
σ_{τ_i}	Error in proper decay time
Ω_i	Transversity angles $\Omega_i = (\theta_{T_i}, \phi_{T_i}, \psi_{T_i})$
$P_i(B\|Q_x)$	Per candidate tagging probability
p_{T_i}	Transverse momentum

At large τ_i, an inefficiency is caused by trigger-matched muons with high transverse impact parameter, affected by the tracking acceptance. This is accounted for by reweighting events in the fit by:

$$w = p_0 \cdot \left[1 - p_1 \cdot \left(\text{Erf}\frac{\tau - p_3}{p_2} + 1\right)\right] \tag{3.6}$$

Where the p_i are determined in a fit to Monte Carlo (MC) events. Calibrations from a $B^\pm \to J/\psi K^\pm$ sample are used to determine a per candidate probability of the candidate was produced as a B_s^0 given a *cone charge* Q_x, the track(s) charge in a particular region, used as a 'tagging decision' (See chapter 4).

3.3.1 The Signal Probability Distribution Function

The signal probability distribution used is given by:

$$\begin{aligned}\mathcal{F}_s =& P_s(m_i|\sigma_{m_i}) \cdot P_s(\sigma_{m_i}|p_{T_i}) \cdot P_s(\tau_i, \Omega_i|\sigma_{\tau_i}, P_i(B|Q_x)) \\ & \cdot P_s(\sigma_{\tau_i}|p_{T_i}) \cdot P_s(P_i(B|Q_x)) \cdot A(\Omega_i, p_{T_i}) \cdot P_s(p_{T_i})\end{aligned} \tag{3.7}$$

The mass term is modelled by a Gaussian function:

$$P_s(m_i|\sigma_{m_i}) = \frac{1}{S_m\sigma_{m_i}\sqrt{2\pi}} e^{\frac{-(m_i - m_{B_s^0})^2}{2(S_m\sigma_{m_i})^2}} \tag{3.8}$$

The term σ_{m_i} is calculated from the covariance matrix of the vertex fit. The S_m accounts for errors in the measurement, which along with the self explanatory $m_{B_s^0}$ is determined by the fit. The three terms $P_s(\sigma_{m_i}|p_{T_i})$, $P_s(\sigma_{\tau_i}|p_{T_i})$ and $P_s(p_{T_i})$ serve to account for the differences in the mass, proper decay time and transverse momentum between signal and background events. Their respective distributions may be represented by[4] [23]:

$$P_{s(b)}(\sigma_{t(m_i)}) = \frac{(\sigma_{t(m_i)} - c)^{a_{s,b}} e^{-(\sigma_{t(m_i)} - c)/b_{s,b}}}{b_{s,b}^{a_{s,b}+1}\Gamma(a_{s,b}+1)} \tag{3.9}$$

The constants $a_{s,b}$ and $b_{s,b}$ are determined by the fit in the (b) side-bands and (s) background-subtracted signal[5]. The same apparatus is used for the p_T distributions, with different values of the fit parameters. The joint PDF $P_s(\tau_i, \Omega_i|\sigma_{\tau_i}, P_i(B|Q_x))$ encodes the decay time resolution, convoluting each time element in Table 3.1 by a Gaussian on a per-event basis. The average value of this uncertainty in the signal is 64 fs. The decay time distribution is modelled by an exponential smeared by per-event Gaussian errors.

As derived and reported in [27] the $B_s^0 \to J/\psi\phi$ PDF is symmetric under the simultaneous transformations:

$$\{\phi_s, \Gamma_s, \delta_\perp, \delta_{||}\} \to \{\pi - \phi_s, -\Gamma_s, \pi - \delta_\perp, 2\pi - \delta_{||}\} \tag{3.10}$$

The term $A(\Omega_i, p_{T_i})$ is called the acceptance function. Its purpose is to include the angular acceptance of the detector, and kinematic cuts on the the Ω distributions. It is determined by a 4D binned acceptance method, with p_T and Ω based event-by-event efficiency corrections in $B_s^0 \to J/\psi\phi$ MC[6] events. The acceptance and decay PDF are normalised numerically together during the likelihood fit, over the mass range 5150-5650 MeV. The signal mass region for the fit $|m_i - 5366| < 50$ MeV.

[4] The subscript b stands for 'background', discussed in section 3.3.2

[5] Also, discussed in section 3.3.2 and section 4.3

[6] The Monte Carlo is discussed in section 3.3.3

3.3.2 The Background Probability Distribution Function

The background PDF is built as:

$$\begin{aligned}\mathcal{F}_{\text{bkg}} =& P_b(m_i)\cdot P_b(t_i|\sigma_{t_i})\cdot P_b(P_i(B|Q_x))\\ &\cdot P_b(\Omega_i)\cdot P_b(\sigma_{m_i}|p_{T_i})\cdot P_b(\sigma_{\tau_i}|p_{T_i})\cdot P_b(p_{T_i})\end{aligned} \tag{3.11}$$

Here, $P_b(m_i)$ is modelled by an exponential function plus a constant, $P_b(\tau_i|\sigma_{\tau_i})$ is modelled by a Gaussian peak, and 3 exponentials – two positive time, and one negative. The peak describes so called prompt[7] combinatorial events with reconstructed τ_i around the zero mark, the positive exponentials model higher lifetime background events with J/ψ particles not from the main collision, combined with B or D hadrons in the same event or with prompt hadron tracks associated with the primary vertex. The negative exponential function represents events with worse vertex resolution. $P_b(\sigma_{m_i}|p_{T_i})$, $P_b(\sigma_{\tau_i}|p_{T_i})$ and $P_b(p_{T_i})$ were defined in equation 3.9. The PDF $P_b(\Omega_i)$ has strong dependence on detector and kinematic acceptance, and is built from the Legendre polynomials as follows:

$$\begin{aligned}Y_l^m(\theta_T) =& \sqrt{(2l+1)/(4\pi)}\sqrt{(l-m)!/(l+m)!}P_l^{|m|}(\cos\theta_T)\\ P_k(x) =& \frac{1}{2^k k!}\frac{d^k}{dx^k}(x^2-1)^k \qquad \text{where } x=\cos\psi_T\\ \mathscr{P}_b(\Omega) =& \sum_{k=0}^{14}\sum_{l=0}^{14}\sum_{m=-l}^{l}\begin{cases} a_{k,l,m}\sqrt{2}Y_l^m(\theta_T)\cos(m\phi_T)P_k(x) & m>0\\ a_{k,l,m}\sqrt{2}Y_l^{-m}(\theta_T)\sin(m\phi_T)P_k(x) & m<0\\ a_{k,l,m}\sqrt{2}Y_l^0(\theta_T)P_k(x) & m=0\end{cases}\end{aligned} \tag{3.12}$$

The $a_{k,l,m}$ are tuned for the best angular distribution fit in the side-band regions, which are defined by $5150 < m_i < 5316$ and $5416 < m_i < 5650$. The terms $\mathcal{F}_{B^0}$ and $\mathcal{F}_{\Lambda_b}$ (See 3.2), account for the possibility of $B_d^0 \to J/\psi K^{*0}$ and $\Lambda_b \to J/\psi p K^-$ being mistakenly reconstructed as $B_s^0 \to J/\psi\phi$ events. Relative to signal candidates, the fractions f_{B^0} and f_{Λ_b}, evaluated in the MC are:

$$\begin{aligned}f_{B^0} =& (4.3\pm 0.5)\%\\ f_{\Lambda_b} =& (2.1\pm 0.6)\%\end{aligned} \tag{3.13}$$

Contributions from the interference of S-wave $B_d^0 \to J/\psi K^+\pi^-$ and P-wave $B_d^0 \to J/\psi K^{*0}$ are included in the PDF with the parameters taken from [28]. We now turn to an overview of the Monte Carlo that has been mentioned at several points over the description of the maximum likelihood fit.

[7] Originating from the main collision event

3.3.3 Outline of the Monte Carlo

A 100M Monte Carlo $B_s^0 \to J/\psi\phi$ events were generated using `PYTHIA 8.210` tuned with ATLAS data for evaluation of backgrounds, detector response and systematic effects. Additionally $B_d^0 \to J/\psi K^{*0}$ and $\Lambda_b \to J/\psi p K^-$ and inclusive $b\bar{b} \to J/\psi X$ and $pp \to J/\psi X$ background samples were simulated. Exclusive $B^\pm \to J/\psi K^\pm$ were generated for calibration of tagging algorithms.

While a detailed explanation of the parameters used, their tuning, and the working of the simulation is outside the purview of this work, nonetheless, the reader is referred to the relevant literature below:

- The Preprint *"Measurement of the CP-violating phase ϕ_s and other $B_s^0 - \overline{B}_s^0$ mixing parameters in $B_s^0 \to J/\psi\phi$ decays in ATLAS at $\sqrt{s} = 13$ TeV"* [26].
- The parameter values used are the 'A14' set discussed in *"ATLAS PYTHIA 8 tunes to 7 TeV data"* [29].
- The 'A14' tune is based on the Monash tune, which may be found in *"Tuning PYTHIA 8.1: the Monash 2013 tune"* [30] with simultaneous variation of 10 parameters.
- The CTEQ6L1 parton functions, given in *"New Generation of Parton Distributions with Uncertainties from Global QCD Analysis"* [31].
- The details of the tuned parameters may be found in the `PYTHIA 8` Online Documentation or *"A comprehensive guide to the physics and usage of PYTHIA 8.3"* [32].

Chapter 4

Same side $K^{\pm}$ tagger & characterisation methodology

Having understood the motivations of this study, and the application of the developed algorithm, namely its role in the study of the $B_s^0 \to J/\psi\phi$ decay through the partial wave analysis fit, discussed in chapter 3, we may now finally get to the discussion of the same side $K^{\pm}$ tagging (SSKT), and the techniques used to evaluate its effectiveness. We first discuss some key definitions in section 4.1, then the principle and working of the algorithm in section 4.2 and finally the methodology of its characterisation in section 4.3.

4.1 Definitions

Before a discussion of the principle and characterisation, it is important the develop the necessary jargon and terminology that will be used hereafter.

A *Same Side Tagger* is a method of tagging the B_s^0, using information from hadronisation of particles associated with the signal meson.

An *Opposite Side Tagger* is a method of tagging the B_s^0, using information from the decay chain of the opposite b-quark formed in the $b\bar{b}$ pair.

The *Cone*, usually referred to is a is a conic volume, defined around the track (lepton, or jet) axis, defined by the radius $\Delta R = \sqrt{(\Delta\phi)^2 + (\Delta\eta)^2}$.

The *Cone Charge*, $-1 \leq Q_x \leq 1$ is defined as the weighted sum of the charge of the tracks that lie within the cone. Here $x = \{e, \mu, K^{\pm}\}$. Explicitly:

$$Q_x = \frac{\sum_{i=1}^{N_{\text{tracks}}} q_i \cdot (p_{T_i})^{\kappa}}{\sum_{i=1}^{N_{\text{tracks}}} (p_{T_i})^{\kappa}} \tag{4.1}$$

where the ΔR and κ depend on an optimisation and are different for different methods. The Q_x is further subdivided into *continuous* $-1 < Q_x < 1$ and *discrete* $Q_x = \pm 1$ regions. The SSKT developed mainly uses discrete Q_x.

The *Tagging decision*, d is the output of the tagging algorithm, usually the cone charge, Q_x which helps infer the flavouring.

The *efficiency*, ϵ_x of the tagger is the fraction of signal events tagged by the algorithm in question:

$$\epsilon_x = \frac{\text{Number of correctly and incorrectly tagged events}}{\text{Total number of signal events}} \tag{4.2}$$

The *dilution* is a measure of the quality of discrimination of $b/\overline{b}$ by the algorithm. Is is the difference of the probability of correct tagging $P(B_s|d)$ and the probability of a mistag $P(\overline{B}_s|d)$ or ω, denoted as:

$$\mathcal{D}_x = P(B_s|d) - P(\overline{B}_s|d) = 2P(B_s|d) - 1 = (1 - 2\omega) \tag{4.3}$$

If we recall equation 1.39, the decay rates that define the interference CP-asymmetry $A_{\mathrm{CP},J/\psi\phi}(t)$ would in practice be measured as:

$$\begin{aligned}\Gamma^m(B_s^0 \to J/\psi\phi) =& \epsilon_{\mathrm{t}}[(1-\omega_{\mathrm{t}})\Gamma(B_s^0 \to J/\psi\phi) + \omega_{\mathrm{t}}\Gamma(\overline{B}_s^0 \to J/\psi\phi)] \\ \Gamma^m(\overline{B}_s^0 \to J/\psi\phi) =& \epsilon_{\mathrm{t}}[(1-\omega_{\mathrm{t}})\Gamma(\overline{B}_s^0 \to J/\psi\phi) + \omega_{\mathrm{t}}\Gamma(B_s^0 \to J/\psi\phi)]\end{aligned} \tag{4.4}$$

where, the superscript, m denotes 'measured' and the subscript, t stands for 'total', that is, the total efficiency and mistag of all taggers used. This has the following 'diluting' effect on the measured asymmetry:

$$\begin{aligned}A^m_{\mathrm{CP},J/\psi\phi}(t) =& \frac{\Gamma^m(B_s^0 \to J/\psi\phi) - \Gamma^m(\overline{B}_s^0 \to J/\psi\phi)}{\Gamma^m(B_s^0 \to J/\psi\phi) + \Gamma^m(\overline{B}_s^0 \to J/\psi\phi)} \\ =& (1-2\omega)A_{\mathrm{CP},J/\psi\phi}(t) = \mathcal{D} \cdot A_{\mathrm{CP},J/\psi\phi}(t)\end{aligned} \tag{4.5}$$

Lastly, the *tagging power*, T_x is an overall qualifier of a given tagger, defined using the efficiency and dilution together as follows:

$$T_x = \sum_i \epsilon_{x,i} \cdot \mathcal{D}^2_{x,i} \tag{4.6}$$

where the sum is over the Q_x intervals -1, (-1,1) and +1.

4.2 Same side $K^{\pm}$ tagging

The above defined same side and opposite side terms can be more clearly visualised in Fig. 4.1. In the hadronisation of the $\overline{b}$ into the signal B_s^0, the s-quark is captured from vacuum $s\overline{s}$ pair. The second $\overline{s}$ associated with the signal B_s^0 that remains, then may hadronise with accompanying light quarks and form a

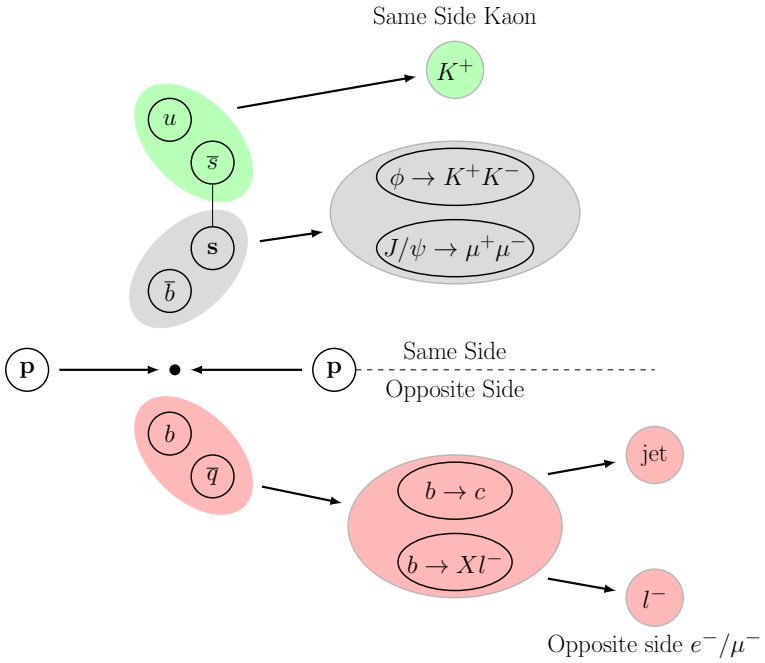

Figure 4.1: Hadronisation associated with a signal $B_s^0 \to J/\psi\phi$ event (grey), into a charged kaon (green) on the same side, and various leptopnic or hadronic tracks (red) on the opposite side. The K^+ indicates a $(\overline{b}s)$ flavour at creation.

charged kaon about 50% of the time [33]. The association of the flavouring with the charge is: a $K^+(u\overline{s})$ meson tags B_s^0, while a $K^-(\overline{u}s)$ then tags the antiparticle $\overline{B}_s^0$. It is also possible for the B_s^0 meson to be associated with a neutral strange particle, such as a K^{*0} (which would lead to a right-sign K) or a Λ. In this work, we investigate the quality and applicability of tagging based on this principle on the unidentified hadronic tracks associated with the B_s^0 mesons in the full ATLAS Run-2 data set corresponding to 139 fb^{-1} of integrated luminosity. The tracks must be close to the phase space of the signal B_s^0 particle, for this tracks that lie within the narrow cone defined by $\Delta R < 0.1$ are considered where the contamination from background events is expected to be low.

The algorithm applied runs a loop over all the best χ^2 selected events, at total of 6,530,361. The following selection criteria is employed:

1. Check for a track associated to the B_s^0 event in the narrow $\Delta R < 0.1$ cone.
2. Construct a 4-momentum vector, with the tracks' 3-momentum (p_T, η, ϕ) and a charged kaon's mass, 493.6 MeV.
3. Apply a transverse momentum to suppress background, the requirement $p_T > 1000$ MeV is imposed.

4. Apply selection to retain only 'rapid' tracks. This 'rapidity discrimination' is defined in the following way:
   (a) Boost the 4-momentum of the track to the rest frame of the system of the B_s^0+track.
   (b) Chose candidates in the so called 'forward hemisphere' by selecting those candidates, whose 3-momentum vector in the boosted frame of reference makes an acute angle with the B_s^0+track momentum in the lab frame.
5. Run a loop over the tracks, storing the count of tracks associated with the given signal event in a counter weighted by p_{T_i} in `same_jet_count_pT` and add up the charge of each track in a second counter `same_jet_sum_pT`, also weighted by p_{T_i}.
6. Divide `same_jet_sum_pT`/`same_jet_count_pT` to obtain the cone charge, Q_{SSK} for the same side kaon tagger.
7. Return the decision as $d = Q_{\mathrm{SSK}}$, i.e. B_s^0 in case of positive charge and $\overline{B}_s^0$ in case of negative.

In practice, the p_{T_i} weighting was found not to have any effect, since for the most part, only single tracks passed the selection criteria, leaving the average cone charge as simply the charge of the track. Therefore the weighting and "`_pT`" suffixes may be dropped, that is one may set $\kappa = 0$. Essentially this means unlike the other opposite side taggers (OSTs), where the cone charge intervals were divided into a continuous $-1 < Q_x < +1$ and two discrete $Q_x = \pm 1$ cases (referred to as 'spikes' in the jargon), in the case of the SSKT, we only deal with the discrete zones of the PDF $P(B|d)_{\mathrm{SSK}}$.

An event that either does not have a track associated to the signal in the $\Delta R < 0.1$ cone or a track that passed the p_{T_i} and rapidity discrimination is considered untagged an assigned a probability of 0.5 in the maximum likelihood fit. While the OSTs, by definition (See Fig. 4.1) should not have any overlap, they may have an overlap with the SSKT, or any same side tagger (SST). This advantage would allow the usage of a 'combination' or 'double' tagging, in the following manner:

$$\begin{aligned} p(\bar{b}s) &= \prod_i \left(\frac{1 - d_i}{2} + d_i(1 - \omega_i) \right) \\ p(b\bar{s}) &= \prod_i \left(\frac{1 + d_i}{2} - d_i(1 - \omega_i) \right) \end{aligned} \tag{4.7}$$

where d_i is the decision of the i^{th} tagger, set to +1 for B_s^0 and -1 for $\overline{B}_s^0$, and

the probabilities renormalised as:

$$P(\bar{b}s) = \frac{p(\bar{b}s)}{p(\bar{b}s) + p(b\bar{s})} \qquad P(b\bar{s}) = 1 - P(\bar{b}s) \tag{4.8}$$

The combination tagging decision is taken as:

- Claim B_s^0, $d_c = +1$ if $P(\bar{b}s) > P(b\bar{s})$
- Claim $\overline{B}_s^0$, $d_c = -1$ if $P(\bar{b}s) < P(b\bar{s})$.

4.3 Characterisation

While the OSTs were calibrated for their discrimination quality using $B^{\pm} \to J/\psi K^{\pm}$ as stated in section 3.3, the SSKT algorithm needs to be analysed differently. The technique used in this work exploits the SSKT+OST double tagging using two semileptopnic OSTs, electron tagger and tight muon tagger to evaluate the SSKT's qualifiers, $\mathcal{D}_{\text{SSK}}$ and $\mathcal{T}_{\text{SSK}}$ by calibration using the already known OST calibrations.

4.3.1 Regions of interest

First, we look at the distribution of all events over the analysed mass range, and the distribution of events tagged by electrons, tight muons and the strange hadron tracks associated to the signal event in Fig. 4.2. In all cases we see the expected peak right around the average B_s^0 mass of 5366 MeV along with the exponential background mentioned in section 3.3.2. Over a small range around the peak (5366$\pm$100 MeV), the background distribution does not differ significantly from a linear function, and we make use of a *side-band subtraction* to retain just the normally distributed signal events, that is a range $m_i \in (5316, 5416)$ is defined as the peak region (signal+background), and the range $m_i \in (5266, 5316) \cup (5416, 5466)$ as the side-band region (background). The events in the side-bands enable a modelling of the background in the peak region, which may then be subtracted from the PDFs built from the peak region events to define a background-subtracted 'signal' result. Determination of the efficiency, ϵ_{SSK} of the SSKT is simple: the fraction of *signal* events that pass the selection criteria to the total number of *signal* events in the data set. So we may directly write:

$$\epsilon_{\text{SSK}} = \frac{\text{No. of tagged peak events} - \text{No. of tagged side-band events}}{\text{No. of peak events} - \text{No. of side-band events}}$$

$$\epsilon_{\text{peak(bkg)}} = \frac{\text{No. of tagged peak (side-band) events}}{\text{No. of peak (side-band) events}} \tag{4.9}$$

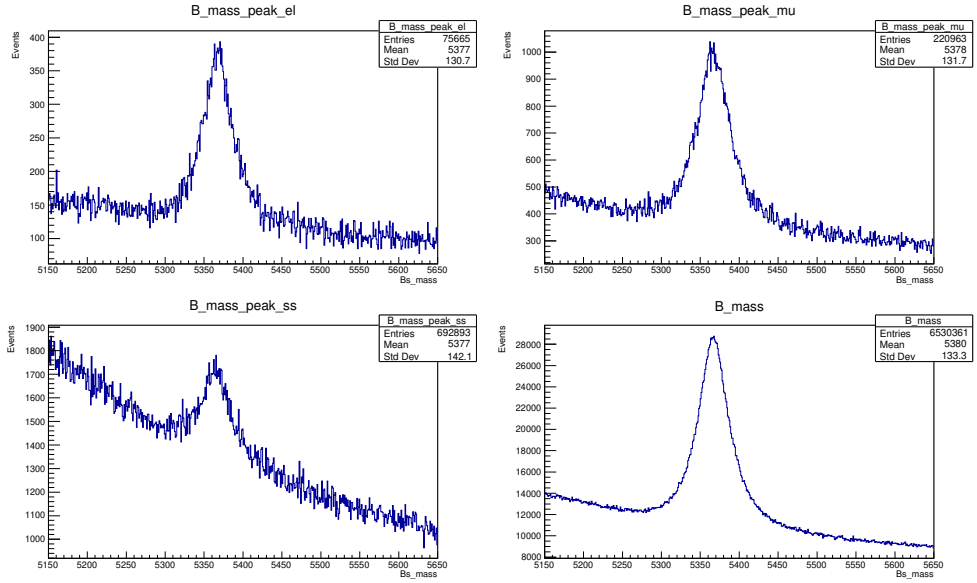

Figure 4.2: Distribution of analysed events over the mass range 5150-5650 MeV of the electon tagged events (top left), muon tagged events (top right), SSKT tagged events (bottom left), and the plain distribution of all events tagged and untagged (bottom right).

4.3.2 Calibration Opposite Side Taggers

The $P(B|Q_x)$ PDFs of the OSTs used to qualify the discrimination of the SSKT using a double tagging approach, described in section 4.3.3 can be seen in Fig. 4.3.

Tracks are identified as electrons using information from the ID and calorimeter. They are required to classified as *medium electrons* (See [34]) and have $p_{T_i} > 2.5$ GeV, $|\Delta z| < 0.5$ mm. If the opening angle between the electron's and B meson's 3-momentums ζ_b, is such that $\cos\zeta_b > 0.93$ it is discarded to exclude signal side decay electrons. The cone charge Q_e is calculated using $\kappa = 1.0$ in equation 4.1 and with ID tracks in the range $\Delta R < 0.5$ and $p_{T_i} > 0.5$ GeV.

The tight muon candidate tracks are reconstructed sacrificing some efficiency giving priority to the purity of the muons, hits in two stations of the MS of combined muons and further criteria given in [35]. They dominate the range $p_{T_i} > 4$. The additional muons used for tagging, are required to have $p_{T_i} > 2.5$ GeV, $|\Delta z| < 0.5$ mm (primary vertex and longitudinal impact parameter of muon associated ID track difference), and $|\eta| < 2.5$. The cone charge Q_μ is calculated using $\kappa = 1.1$ in equation 4.1 and summing over ID tracks in the range $\Delta R < 0.5$ and $p_{T_i} > 0.5$ GeV while excluding tracks associated with the signal decay. In both cases when multiple muons or electrons pass the selection, the highest p_{T_i} candidate is chosen.

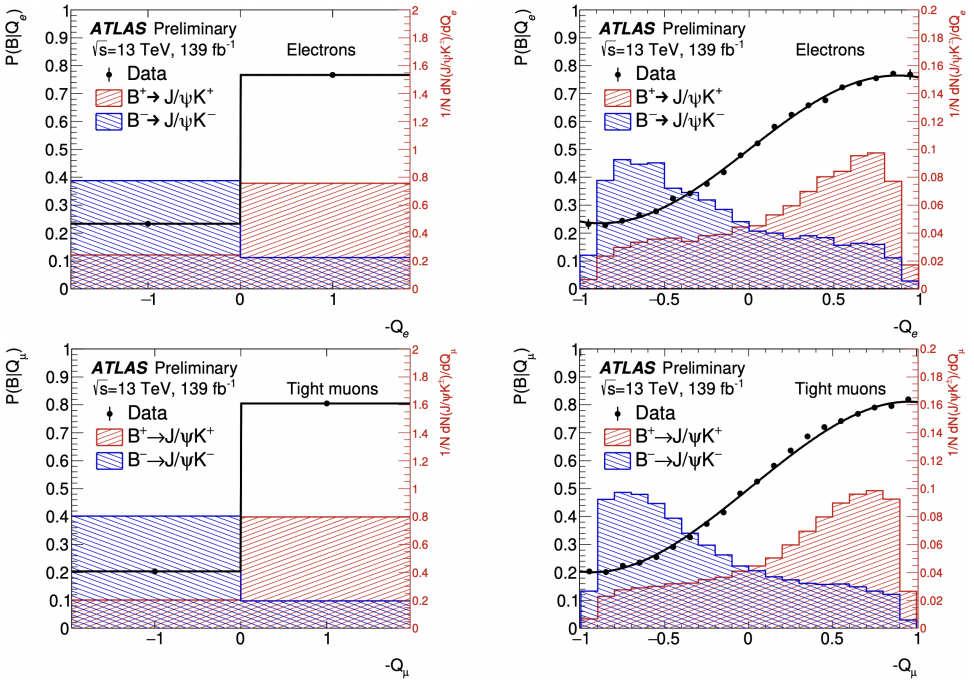

Figure 4.3: The cone charge distributions, $-Q_e$ (top) and $-Q_\mu$ (bottom), shown for both the discrete charge (left), and for the continuous distribution (right). In red (blue), the normalised B^+ (B^-) Q_x distribution is shown (right axis scale). The negative $-Q_{\mu(e)}$ is included to illustrate more B^+ like candidates to the right of the horizontal axis. Overlaid is the tagging PDF, $P(B|Q_{\mu(e)})$, as a function of the cone charge, derived from the $B^\pm \to J/\psi K^\pm$ data sample, and defined as the probability to have a B^+ on the signal-side given $Q_{\mu(e)}$. The black curve is the fitted parameterisation used as a calibration curve to infer the probability to have a $B_s^0(\overline{B}_s^0)$ at production in the decays to $J/\psi\phi$ [26].

4.3.3 Combination Tag Calculation of Dilution

In order to determine the discrimination or purity of the SSKT, a so called *combination* or *double tag* approach was used. The distributions of events tagged by both an OST and the SSKT can be seen in Fig. 4.4. The procedure is:

1. Divide all events into the peak and side-band categories.
2. Distribute SSKT decisions $d_{\text{SSK}} = \pm 1$ into eight histograms:
   (a) `el_tag_pos(_side)`: $-Q_e > 0$
   (b) `el_tag_neg(_side)`: $-Q_e < 0$
   (c) `mu_tag_pos(_side)`: $-Q_\mu > 0$
   (d) `mu_tag_neg(_side)`: $-Q_\mu < 0$

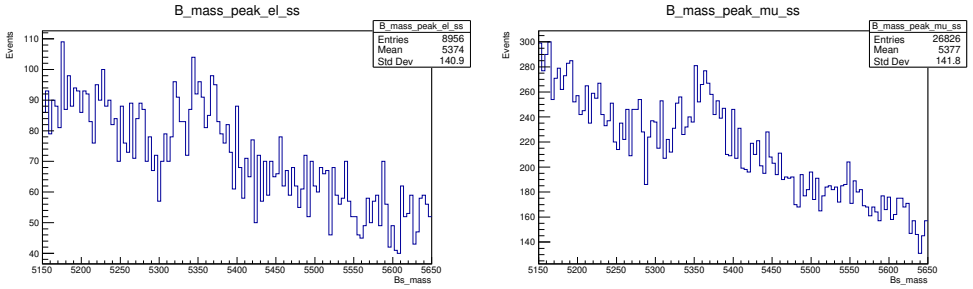

Figure 4.4: Mass distribution of events tagged by a combination of either elections (left) or muons (right) and the SSKT

3. Subtract the `_side` type of distributions from the regular (peak region) histograms to create `_sig` (background-subtracted) histograms.

4. Consider that the number of entries in the +1 bin of the 'pos' type and the number of entries in the -1 bin of the 'neg' type `_sig` histograms are the number of cases of agreement between both taggers, conversely the number of entries in the -1 bin of the 'pos' type and the number of entries in the +1 bin of the 'neg' type `_sig` histograms are the number of cases of disagreement between both taggers. Note, for any combined tagging decision d_c, say +1 the product of dilutions is:

$$\mathcal{D}_{\text{SSK}} \cdot \mathcal{D}_x = [P_{\text{SSK}}(B_s^0|d_c) - P_{\text{SSK}}(\overline{B}_s^0|d_c)][(P_x(B_s^0|d_c) - P_x(\overline{B}_s^0|d_c))] \quad (4.10)$$

That is, the sum of the probabilities of concurrent decisions minus the sum of the probabilities of opposite decisions.

5. Calculate the SSKT dilution as:

$$\frac{\mathcal{D}_{\text{SSK}} \cdot \mathcal{D}_x}{\mathcal{D}_x} = \frac{\text{No. of agreements} - \text{No. of disagreements}}{\text{No. of agreements} + \text{No. of disagreements}} \div \mathcal{D}_x \quad (4.11)$$

This is equivalent to setting $-Q_x > 0 \implies d_x = +1$ and conversely $-Q_x < 0 \implies d_x = -1$ and summing for all signal events:

$$\mathcal{D}_{\text{SSK}} = \frac{\sum_{i=1}^{N_{\text{events}}^{\text{sig}}} d_{x,i} \cdot d_{\text{SSK},i}}{\sum_{i=1}^{N_{\text{events}}^{\text{sig}}} |d_{x,i} \cdot d_{\text{SSK},i}|} \div \mathcal{D}_x \quad (4.12)$$

Finally, the SSKT was deployed as a new tagger to the existing partial wave analysis angular fit code in analogy with existing methods, and the fit was run, the various fit parameters are reported in the results.

Chapter 5

Results and Discussion

This chapter presents a walk-through of the results obtained over the studies of the quality of the same side tagger, described over this thesis hitherto and measurements of the various fit parameters ϕ_s, Γ_s, Δm_s, $\Delta\Gamma_s$ and helicity amplitudes. The final background subtracted results of the tagging quality are presented in subsection 5.1.3 and fit results with SSKT added in Table 5.3. Section 5.1 contains the results of the tagging quality, while section 5.2 the measurements of the angular fit parameters. The mass and proper decay time distributions of the analysed data sample are depicted in Fig. 5.1.

5.1 SSKT Quality Measurements

We begin with short note on rejection of background candidates in subsection 5.1.1, and then go over the measurements in the peak and side-band regions, in subsections 5.1.2. This section is then concluded with the background-subtracted measurements of the efficiency, dilution and tagging power in subsection 5.1.3.

5.1.1 Rejection of background candidates

As is clearly visible in Fig. 5.2 and Fig. 5.3, the Q_{SSK} is concentrated in the ± 1 bins (spikes), which is the charge interval studied further in this work. Furthermore, Fig. 5.4 shows the difference between SSKT tagged events considering any Q_{SSK} spike events as tagged, and considering only `same_jet_count`=1 spike events (that is to say, one and only one track passed the selection). The rejection of multiple track events lowers the background fraction while retaining $B_s^0 \to J/\psi\phi$ signal events. We henceforth proceed with only single track spikes. Events with $-1 < Q_{\mathrm{SSK}} < +1$ are considered untagged and assigned a probability of 0.5 for the purposes of the fit.

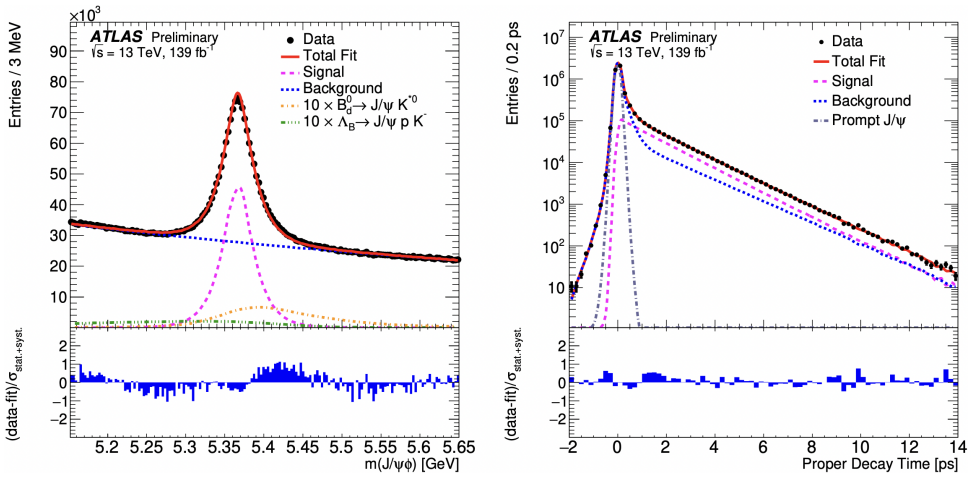

Figure 5.1: Fitted mass distribution of the analysed $B_s^0 \to J/\psi\phi$ sample (Left). The total fit is shown in red, the magenta line shows the $B_s^0 \to J/\psi\phi$ signal, the orange line depicts $\Lambda_b \to J/\psi pK^-$ events. The proper decay time τ of the analysed $B_s^0 \to J/\psi\phi$ sample (Right). The total fit is shown in red, signal in magenta, blue shows the total background and grey the prompt J/ψ background. A ratio plot of the difference between the total fit divided by $\sigma_{\text{stat.+sys.}}$ of each point is given below each figure [26].

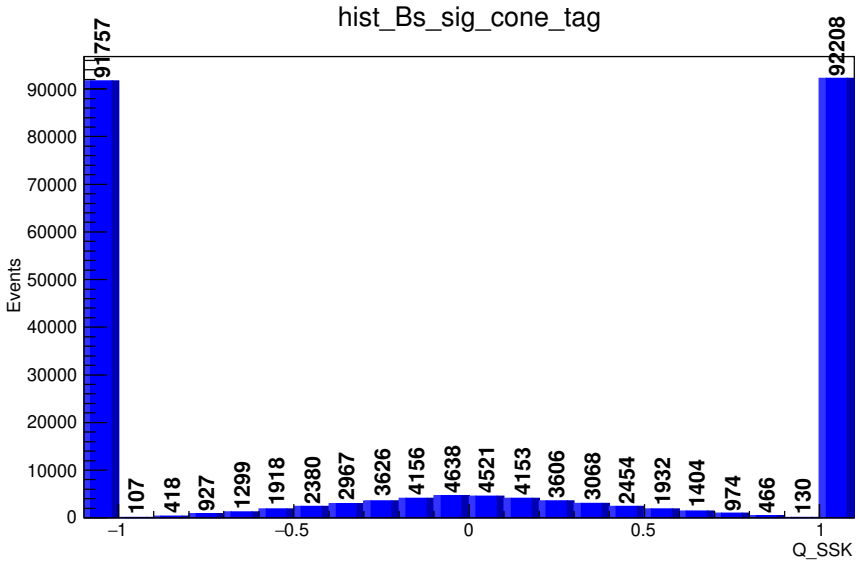

Figure 5.2: Cone charge distribution of same side tracks in the peak region with $m_i \in (5316, 5416)$ [22 bins]. Charge concentrated in $Q_{\text{SSK}} = \pm 1$ intervals.

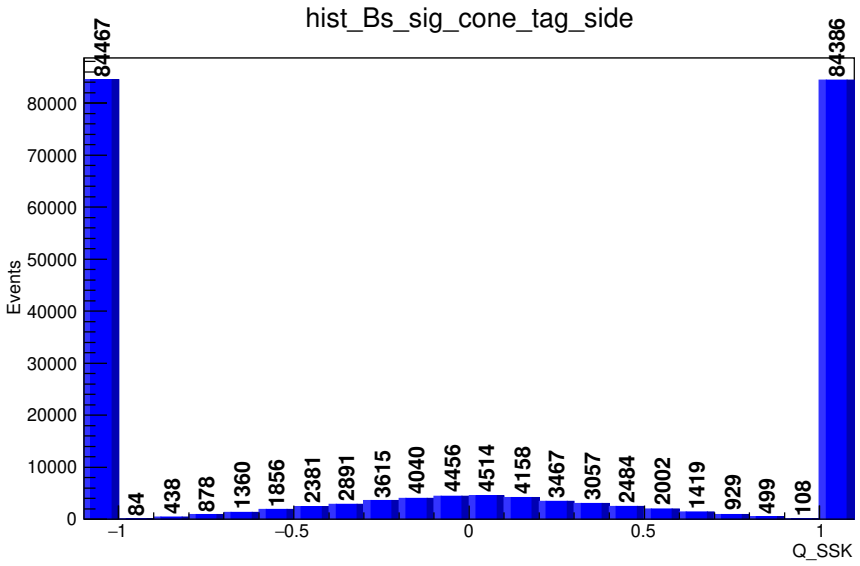

Figure 5.3: Cone charge distribution of same side tracks in the side-band region $m_i \in (5266, 5316) \cup (5416, 5466)$. Charge concentrated in $Q_{\mathrm{SSK}} = \pm 1$ intervals.

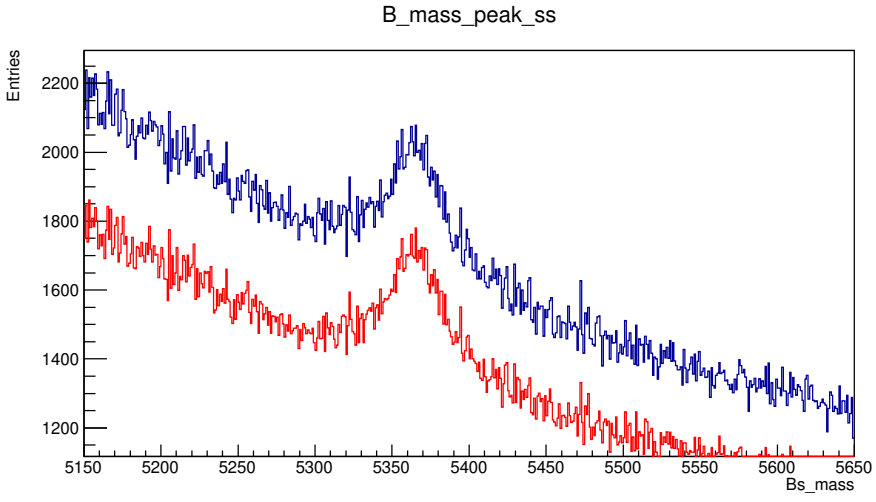

Figure 5.4: The distribution of SSKT tagged events with any $Q_{\mathrm{SSK}} = \pm 1$ considered as tagged (blue) overlaid with the distribution of SSKT tagged events accepting only events with `same_jet_count=1` (red).

5.1.2 Peak & side-band measurements

The peak and side-band region double tag Q_{SSK} distributions are shown in Fig. 5.1.2. The data extracted from these histograms is summarised in Table 5.1.

Table 5.1: Peak and side-band measurements

	Peak Region		Side Bands	
	+1	-1	+1	-1
+Electron	547	506	439	438
-Electron	468	544	432	448
+Muon	1599	1417	1393	1285
-Muon	1395	1575	1344	1408
Q_{SSK} Spikes	77281	76673	69419	69464
Events	2.01156e+06		1.22532e+06	

From this we may calculate, following the formula described in point 5 of section 4.3.3 for the peak without background-subtraction:

$$\begin{aligned} \epsilon_{\mathrm{SSK}}^{\mathrm{peak}} &= (7.65 \pm 0.07 \text{ stat.})\% \\ \mathcal{D}_{\mathrm{SSK}}^{e} &= (12.07 \pm 2.20 \text{ stat.})\% \\ \mathcal{D}_{\mathrm{SSK}}^{\mu} &= (12.78 \pm 1.29 \text{ stat.})\% \\ \mathcal{D}_{\mathrm{SSK}}^{\mathrm{avg}} &= (12.43 \pm 1.75 \text{ stat.})\% \\ \mathcal{T}_{\mathrm{SSK}} &= (0.12 \pm 0.03 \text{ stat.})\% \end{aligned} \tag{5.1}$$

The electron and muon OST dilutions used for these calculations are:

$$\begin{aligned} \mathcal{D}_{e} &= (46.96 \pm 0.17 \text{ stat.})\% \\ \mathcal{D}_{\mu} &= (47.31 \pm 0.14 \text{ stat.})\% \end{aligned} \tag{5.2}$$

The differences in Q_{SSK} spike contents from Fig. 5.3 are due to the rejection of multiple track (`same_jet_count`> 1) candidates.

5.1.3 Background-subtracted signal measurements

Modelling the background in the peak region using the side-bands (that contain mostly background events) following section 4.3.3, the plots obtained are presented in Fig. 5.1.3. Immediately visible is the increase in discrimination. The data and results are summarised in Table 5.2, along with a cross check with multiple candidate tracks.

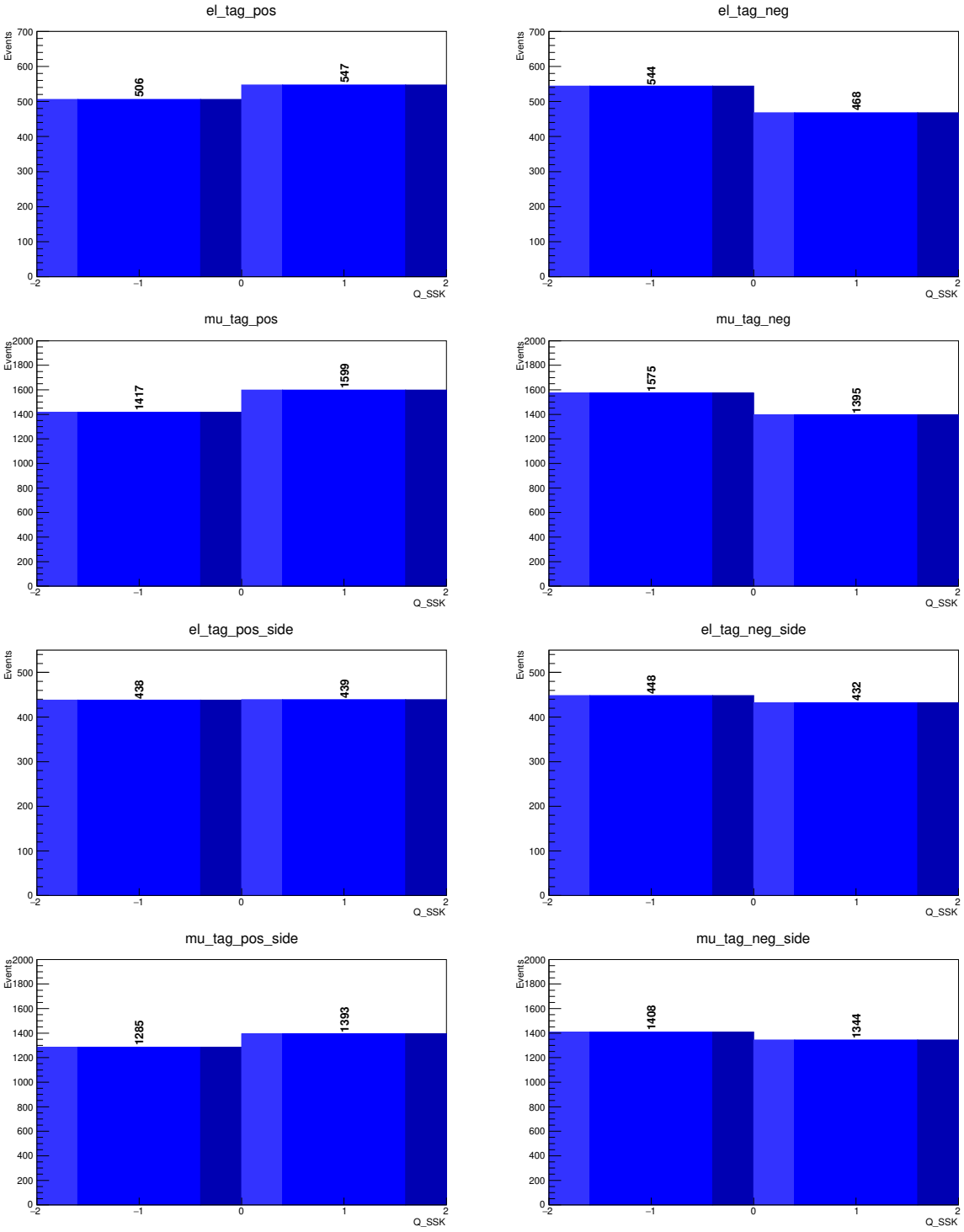

Figure 5.5: Peak and side-band double tag Q_{SSK} distributions

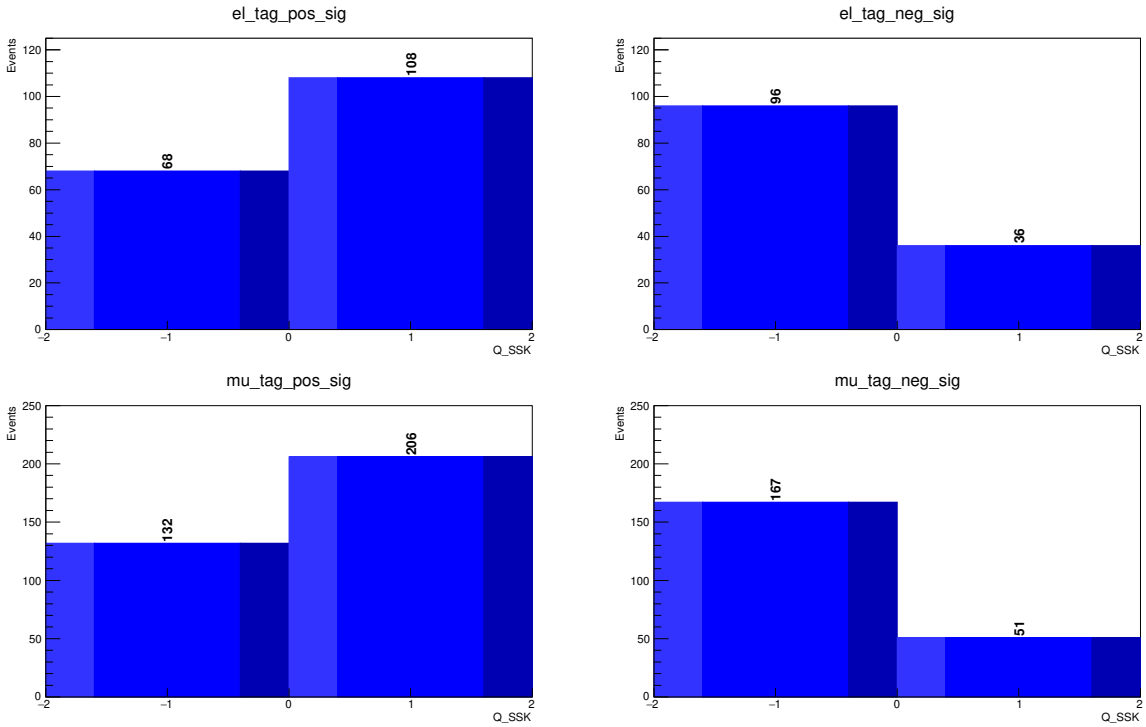

Figure 5.6: Background-subtracted double tag Q_{SSK} distributions

Table 5.2: Background-subtracted signal

Q_{SSK}	+Electron	-Electron	+Muon	-Muon	Spikes
+1	108	36	206	51	7682
-1	68	96	132	167	7209

The qualifying parameters may then be calculated as (See 4.3.3):

$$\begin{aligned}
\epsilon^{\mathrm{sig}}_{\mathrm{SSK}} &= (1.92 \pm 0.11 \text{ stat.})\% \\
\mathcal{D}^{e}_{\mathrm{SSK}} &= (69.14 \pm 5.70 \text{ stat.})\% \\
\mathcal{D}^{\mu}_{\mathrm{SSK}} &= (72.23 \pm 4.24 \text{ stat.})\% \\
\mathcal{D}^{\mathrm{avg}}_{\mathrm{SSK}} &= (70.69 \pm 4.97 \text{ stat.})\% \\
T_{\mathrm{SSK}} &= (0.95 \pm 0.19 \text{ stat.})\%
\end{aligned} \tag{5.3}$$

On allowing multiple track spikes, the efficiency remains the same within rounding error while the discrimination drops to:

$$\begin{aligned}
\mathcal{D}^{e}_{\mathrm{SSK}} &= (53.95 \pm 5.77 \text{ stat.})\% \\
\mathcal{D}^{\mu}_{\mathrm{SSK}} &= (48.21 \pm 4.19 \text{ stat.})\%
\end{aligned} \tag{5.4}$$

5.2 Fit Parameter Results

Two runs of the angular fit were run, without the SSKT, and after deployment of the SSKT, the calculated parameters and uncertainties are presented in Table 5.3.

Table 5.3: Results of the angular fit outlined in section 3.3

Parameter	Only OSTs Run		With SSKT Run	
[units]	Value	Error	Value	Error
$\|A_0\|^2$	0.5062	0.0009	0.5062	0.0009
$\|A_{\|\|}\|^2$	0.2264	0.0014	0.2264	0.0014
$\|A_S\|^2$	0.0225	0.0024	0.0225	0.0024
Γ_s [ps^{-1}]	0.6717	0.0011	0.6722	0.0011
$\Delta\Gamma_s$ [ps^{-1}]	0.0648	0.0034	0.0645	0.0034
Δm_s [ps^{-1}]	17.882	0.0409	17.8999	0.1383
ϕ_s [rad]	-0.0640	0.0295	-0.0080	0.0294
$\delta_{\|\|}$ [rad]	3.3998	0.0279	3.4011	0.0278
$\delta_\perp$ [rad]	3.2262	0.0903	3.2747	0.0929
$\delta_{\|\|} - \delta_\perp$ [rad]	-0.2976	0.0409	-0.2961	0.0407
$\|\lambda\|$	0.9999	0.0100	0.9905	0.0145

While the previous measurement of ϕ_s was to the left of the standard model prediction of $\phi_s = -0.03696^{+0.00072}_{-0.00082}$ [36] the new measurement with SSKT information is observed to shift to the right more in line with the value reported by CMS in 2020 [37]. The CP-violation measurements of this study are quoted:

$$\begin{aligned} \phi_s &= -\,0.0080 \pm 0.0294 \text{ (stat.) [rad]} \\ \Gamma_s &= +\,0.6722 \pm 0.0011 \text{ (stat.) [ps}^{-1}\text{]} \\ \Delta\Gamma_s &= +\,0.0645 \pm 0.0034 \text{ (stat.) [ps}^{-1}\text{]} \\ \Delta m_s &= +\,17.8999 \pm 0.1383 \text{ (stat.) [ps}^{-1}\text{]} \end{aligned} \tag{5.5}$$

5.3 Illustrations

A few additional illustrations can be found in this section. In Fig. 5.7 a function $f(x) = p_0 \cdot \exp(p_1 \cdot x + p_2) + p_4 \cdot \text{Gauss}(x, 5366, p_3)$, is fit to the distribution of SSKT tagged events. Fig. 5.3 shows the nature of the asymmetry in the lifetime distributions of B_s^0 and $\overline{B}_s^0$ tagged events fit to $p_0 \cos(p_1 \cdot x + p_2) \cdot e^{p_3 \cdot x}$. The 1D likelihood scans of the fit are shown in Fig. 5.9.

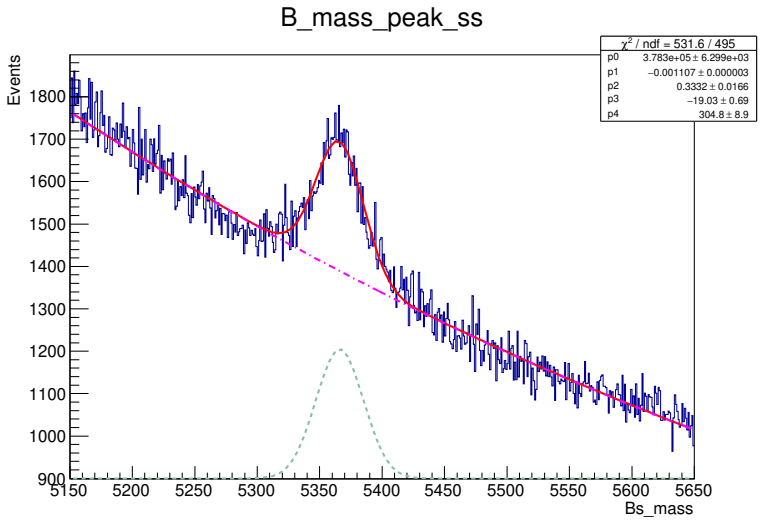

Figure 5.7: Fit to the SSKT tagged events, the total fit is shown in red, the exponential background in magenta, and the signal Gaussian's shape in green. The interval 5366 ± 50 retains over 99% of signal.

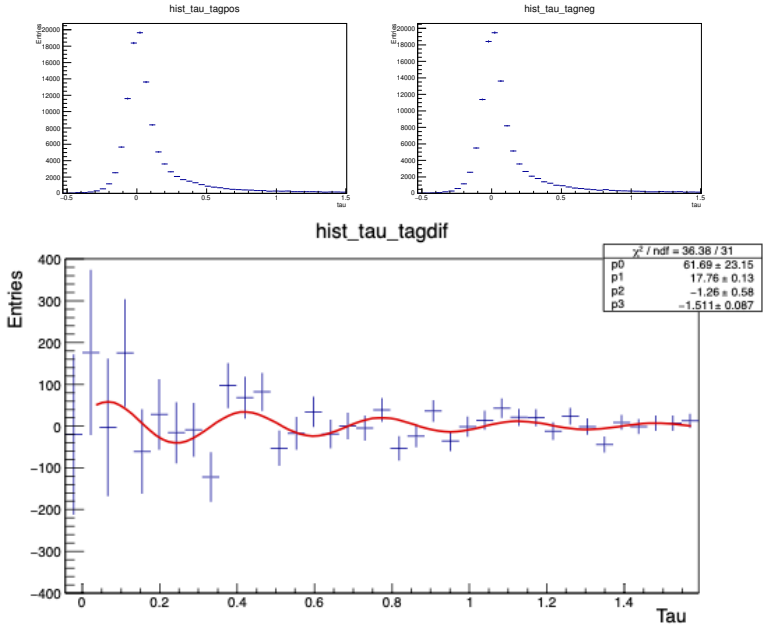

Figure 5.8: The difference (bottom) between lifetime distributions of SSKT particle tagged (top left) and antiparticle tagged (top right) events fitted to a cosine multiplied by a decaying exponential. The mass difference in the cosine (p1) fits to 17.76 ± 0.13 ps^{-1}.

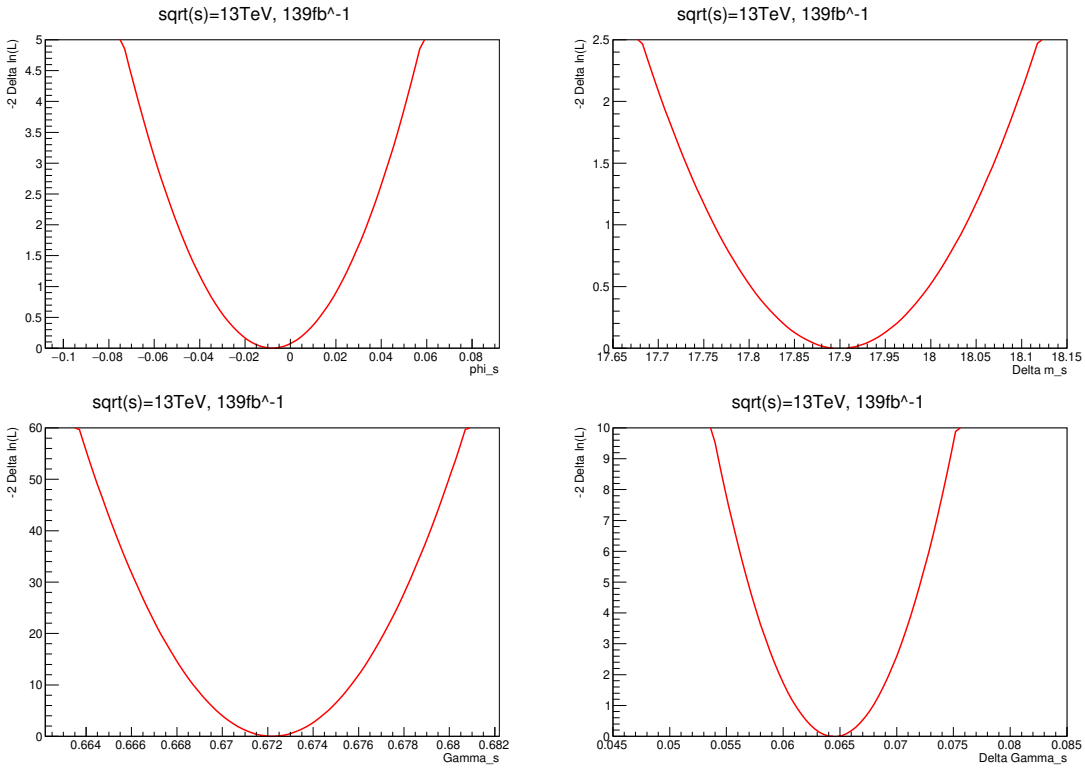

Figure 5.9: 1D log-likelihood scans for the minimum, $\Delta \ln(L) = 2[\ln(L^G) - \ln(L^i)]$ where L^G is the value of the default fit and of the fit in with the parameter fixed to the x-axis value, L^i.

5.4 Concluding remarks

With the above presented illustrations, this work is concluded. In summary, a new algorithm for tagging B_s^0 mesons was developed and tested for quality using the full 2015-18 pp collision, 139 fb^{-1} data set of ATLAS, at $\sqrt{s} = 13$ TeV. Additionally, the algorithm was used alongside previously developed OSTs to measure the time dependant CP-asymmetry parameters. The measured value of $\phi_s = -0.0080 \pm 0.0294$ (stat.) is consistent with the SM prediction [7, 36], and closer to the recent CMS measurement [37]. The direct CP-violation characterised by $|\lambda| = 0.9905 \pm 0.0145$(stat.) is consistent with unity implying no evidence of direct CP-violation.

Fig. 5.10 shows the 2D 68% CL contours of $\Delta\Gamma_s - \phi_s$ along with the measurements from various LHC experiments, modelled as 2D Gaussians accounting for the correlations. The measured $\Delta m_s = 17.8999 \pm 0.1383$ (stat.) is consistent with the world average [3] within statistical error and the 2013 high precision

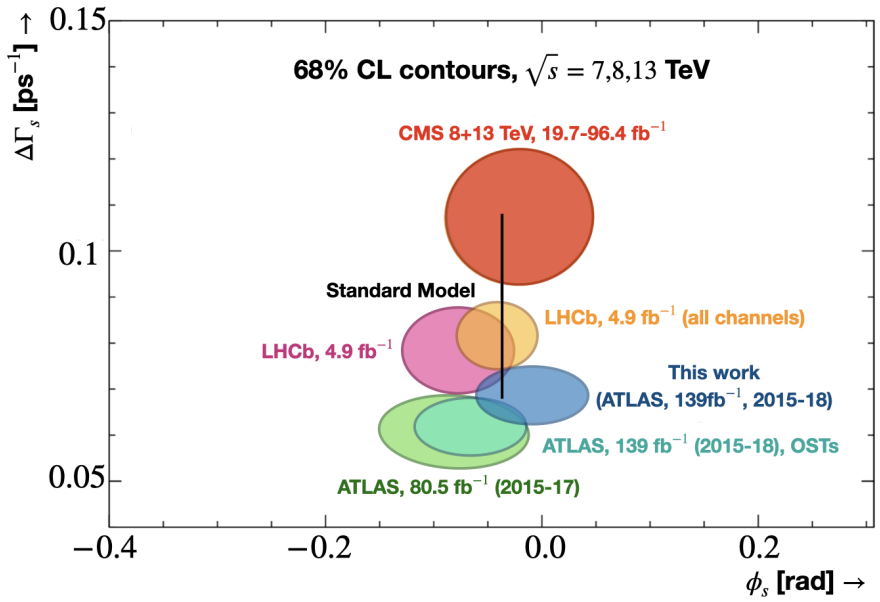

Figure 5.10: Measurements of the 2D constrains on $\Delta\Gamma_s$ and ϕ_s in the previous ATLAS (2015-17) result [39] (light green), ATLAS (2015-18) result (turquoise), LHCb [40] and CMS [41] results compared with the Standard Model prediction [7, 36], and the runs of this work (dark Blue). Uncertainties shown are statistical and systematic, except for the 2015-17 ATLAS run which are only statistical. For the depiction of this work's constrains, systematic uncertainties and correlations are taken to be the same as the 2015-18 OSTs run [26].

measurement of LHCb [38]. Additionally the contributions of systematic uncertainties in the measurements relating to tagging precision, angular acceptance, ID alignment, trigger efficiency, best candidate selection, $P_b(\Omega)$, backgrounds, etc may be considered. The reader is directed to [26] for a detailed description and summarising table of these uncertainties.

In terms of future scope, the developed SSKT algorithm may be further studied with different data samples and sets of selection criteria. Additionally, Λ baryon tagging, currently under development may be integrated along with the available taggers for analysis of the newer Run-3 data, along with the Run-1 and Run-2 data sets.

Bibliography

[1] F. J. Gilman and Y. Nnir, "Quark Mixing: The CKM Picture," in *Annual Review of Nuclear and Particle Science, Stanford Linear Accelerator Center, Stanford University, Stanford, California 94309,* DOI:10.1146/annurev.ns.40.120190.001241, Feb. 1990.

[2] A. Ceccucci, et. al., "CKM Quark-Mixing Matrix," in *Particle Data Group, https://pdg.lbl.gov/2020/reviews/rpp2020-rev-ckm-matrix.pdf*, Jan. 2020.

[3] P.A. Zyla, et. al. (Particle Data Group), "Review of particle physics," in *Prog. Theor. Exp. Phys. 2020, 083C01,* DOI:10.1093/ptep/ptaa104, Aug. 2020.

[4] J. Charles, et. al. (CKMfitter Group), "CP Violation and the CKM Matrix," in *Eur. Phys. J. C41 [hep-ph/0406184],* DOI:10.1140/epjc/s2005-02169-1, Mar. 2005.

[5] A. Hocker et al., "A new approach to a global fit of the CKM matrix," in *Eur. Phys. J. C21, 225 [hep-ph/0104062],* DOI:10.1007/s100520100729, May 2001.

[6] M. Bona et al. (UTfit), "The 2004 UTfit collaboration report on the status of the unitarity triangle in the standard model," in *JHEP 07, 028 (2005), [hep- ph/0501199],* DOI:10.1088/1126-6708/2005/07/028, Feb. 2005.

[7] M. Artuso, et. al., "CP violation in the B_s^0 system," in *Reviews of Modern Physics, arXiv:1511.09466v2 [hep-ph],* DOI:10.48550/ARXIV.1511.09466, Sep. 2019.

[8] Ulrich Nierste, "Three Lectures on Meson Mixing and CKM phenomenology," in *arXiv:0904.1869v1 [hep-ph],* DOI:10.48550/ARXIV.0904.1869, Mar. 2009.

[9] LHC Education, Communications and Outreach Group, "CERN Brochure, 2017-002-Eng," in *home.cern/resources?topic=1119*, Feb. 2017.

[10] L. Arnaudon, et. al., "Linac4 Technical Design Report," in *Technical Report CERN- AB-2006-084. CARE-Note-2006-022-HIPPI, CERN, https://cds.cern.ch/record/1004186/files/ab-2006-084.pdf*, Dec. 2006.

[11] LHC Education, Communications and Outreach Group, "LHC season 2 facts and figures," in *home.cern/resources?topic=1119, accessed*, Jun. 2022.

[12] Christiane Lefèvre, "The CERN accelerator complex," in *CERN Photo-Lab/Physics diagrams and charts*, Dec. 2008.

[13] Jean-Luc Caron, "Cross section of LHC dipole," in *LHC Project Illustrations/Civil engineering*, May 1998.

[14] ATLAS, "Luminosity public results Run-2," in *https://twiki.cern.ch/twiki/bin/view/AtlasPublic/LuminosityPublicResultsRun2, accessed*, Jun. 2022.

[15] ATLAS Collaboration (G. Aad, et. al.), "The ATLAS inner detector commissioning and calibration," in *Eur.Phys.J. C70 (2010), pp. 787–821, DOI: 10.1140/EPJC/ S10052-010-1366-7.*, Aug. 2020.

[16] Joao Pequenao, "Computer generated image of the whole ATLAS detector," in *CERN PhotoLab/Life at CERN*, Mar. 2008.

[17] The ATLAS Collaboration, "Readiness of the atlas liquid argon calorimeter for lhc collisions," in *The European Physical Journal C volume 70, pages 723–753, DOI:10.1140/EPJC/S10052-010-1354-Y*, Aug. 2010.

[18] The ATLAS Collaboration, "Readiness of the atlas tile calorimeter for lhc collisions," in *The European Physical Journal C volume 70, pages 1193–1236, DOI: 10.1140/EPJC/ S10052-010-1508-Y*, Dec. 2010.

[19] The ATLAS Collaboration, "Commissioning of the atlas muon spectrometer with cosmic rays," in *The European Physical Journal C volume 70, pages 875–916, DOI:10.1140/epjc/s10052-010-1415-2*, Oct. 2010.

[20] The ATLAS Collaboration, "Performance of the ATLAS trigger system in 2015," in *Eur. Phys. J. C (2017) 77:317, DOI:10.1140/epjc/s10052-017-4852-3*, Nov. 2016.

[21] Frank Winklmeier, "The atlas run-2 tdaq system," in *ATLAS EXPERIMENT - PUBLIC RESULTS, ApprovedPlotsDAQ*, Jul. 2017.

[22] Werner Herr and Bruno Muratori., "Concept of luminosity," in *CAS - CERN Accelerator School: Intermediate Accelerator Physics, pp.361-378, DOI:10.5170/CERN-2006-002.361*, Apr. 2006.

[23] ATLAS Collaboration (G. Aad, et. al.), "Time-dependent angular analysis of the decay $B_s^0 \to J/\psi\phi$ and extraction of $\Delta\Gamma_s$ and the CP-violating weak phase ϕ_s by ATLAS," in *J. High Energ. Phys. 2012, 72 (2012), DOI:10.1007/jhep12(2012)072*, Aug. 2012.

[24] S.M. Flatté, "Coupled-channel analysis of the $\pi\eta$ and $K\overline{K}$ systems near $K\overline{K}$ threshold," in *Phys. Lett. B 63 (1976) 224 DOI:10.1016/0370-2693(76)90654-7*, Apr. 1976.

[25] Lotte Wilke, "Study of the B_s-Meson with the first LHC data," in *Zurich Open Repository and Archive, DOI:10.5167/uzh-26630*, Jan. 2010.

[26] A. Barton, et. al., "Measurement of the CP-violating phase ϕ_s and other $B_s^0 - \overline{B}_s^0$ mixing parameters in $B_s^0 \to J/\psi\phi$ decays in ATLAS at $\sqrt{s} = 13$ tev," in *ATLAS CONF Note Draft, BPHY-2019-05, Internal documentation, https://cds.cern.ch/record/2703988*, May 2020.

[27] F. Azfar, et. al., "Formulae for the analysis of the flavor-tagged decay $B_s^0 \to J/\psi$," in *Journal of High Energy Physics 2010 (2010), DOI:10.1007/jhep11(2010)158*, Nov. 2010.

[28] LHCb Collaboration (R. Aaij, et. al.), "Measurement of the polarization amplitudes in $B^0 \to J/\psi K^*(892)^0$ decays," in *Phys. Rev. D 88, 052002, DOI:10.1103/physrevd.88.052002*, Sep. 2013.

[29] The ATLAS Collaboration, "ATLAS `PYTHIA` 8 tunes to 7 TeV data," in *CERN Document server*, Nov. 2014.

[30] P. Skands, et. al., "Tuning PYTHIA 8.1: the Monash 2013 tune," in *The European Physical Journal C 74, DOI:10.1140/epjc/s10052-014-3024-y*, Apr. 2014.

[31] J. Pumplin, et. al., "New generation of parton distributions with uncertainties from global QCD analysis," in *Journal of High Energy Physics, DOI:10.1088/1126-6708/2002/07/012*, Jan. 2002.

[32] C. Beirlich, et. al., "A comprehensive guide to the physics and usage of PYTHIA 8.3," in *PYTHIA 8 Online Documentation DOI:10.48550/arXiv.2203.11601*, Mar. 2022.

[33] M. Calvi, et. al., "Flavour tagging algorithms and performances in LHCb," in *CERN Document Server, CERN-LHCB-2007-058, LHCb-2007-058 [INSPIRE Preprint]*, May 2007.

[34] The ATLAS collaboration (G. Aad, et. al.), "Electron and photon performance measurements with the ATLAS detector using the 2015-2017 LHC proton-proton collision data," in *Journal of Instrumentation 14 P12006, DOI:https:10.1088/1748-0221/14/12/P12006*, Dec. 2019.

[35] The ATLAS collaboration (G. Aad, et. al.), "Muon reconstruction performance of the ATLAS detector in proton–proton collision data at $\sqrt{s} = 13$ TeV," in *The European Physical Journal C volume 76, DOI:10.1140/epjc/s10052-016-4120-y*, Mar. 2016.

[36] CKMFitter Group (J. Charles, et. al.), "Current status of the standard model CKM fit and constraints on $\delta f = 2$ new physics," in *Phys. Rev. D 91 (2015) 073007, DOI:10.1103/PhysRevD.91.073007*, Apr. 2015.

[37] CMS Collaboration, "Measurement of the cp violating phase ϕ_s in the $B_s^0 \to J/\psi\phi(1020) \to \mu^+\mu^- K^+K^-$ channel in proton-proton collisions at $\sqrt{s} = 13$ TeV," in *CMS-PAS-BPH-20-001, [INSPIRE]*, Mar. 2020.

[38] LHCb Collaboration, et. al., "Precision measurement of the $B_s^0 - \overline{B}_s^0$ oscillations frequency with the decay $B_s^0 \to D_s^- \pi^+$," in *New J. Phys. 15 053021, DOI:10.1088/1367-2630/15/5/053021*, May 2013.

[39] The ATLAS Collaboration, "Measurement of the CP-violating phase ϕ_s in $B_s^0 \to J/\psi\phi$ decays in ATLAS at 13 TeV," in *Eur. Phys. J. C 81 (2021) 342, DOI:10.1140/epjc/s10052-021-09011-0*, Jan. 2020.

[40] The LHCb Collaboration, "Updated measurement of time-dependent CPviolating observables in $B_s^0 \to J/\psi K^+K^-$ decays," in *The European Physical Journal C volume 79, Article number: 706, DOI:10.1140/epjc/s10052-019-7159-8*, Jun. 2019.

[41] The CMS Collaboration, "Measurement of the CP-violating phase ϕ_s in the $B_s^0 \to J/\psi\phi(1020) \to \mu^+\mu^- K^+K^-$ channel in proton-proton collisions at 13 TeV," in *CMS-PAS-BPH-20-001, https://cds.cern.ch/record/2714363*, Mar. 2020.